



Title	Development of a one-dimensional ecosystem model including the iron cycle applied to the Oyashio region, western subarctic Pacific
Author(s)	Shigemitsu, M.; Okunishi, T.; Nishioka, J.; Sumata, H.; Hashioka, T.; Aita, M. N.; Smith, S. L.; Yoshie, N.; Okada, N.; Yamanaka, Y.
Citation	Journal of Geophysical Research, Oceans, 117, C06021 <a href="https://doi.org/10.1029/2011JC007689">https://doi.org/10.1029/2011JC007689</a>
Issue Date	2012-06-26
Doc URL	<a href="http://hdl.handle.net/2115/50990">http://hdl.handle.net/2115/50990</a>
Rights	©2012 American Geophysical Union
Type	article
File Information	JGR117_C06021.pdf



[Instructions for use](#)

## Development of a one-dimensional ecosystem model including the iron cycle applied to the Oyashio region, western subarctic Pacific

M. Shigemitsu,<sup>1</sup> T. Okunishi,<sup>2</sup> J. Nishioka,<sup>3</sup> H. Sumata,<sup>4</sup> T. Hashioka,<sup>1</sup> M. N. Aita,<sup>5,6</sup> S. L. Smith,<sup>5</sup> N. Yoshie,<sup>7</sup> N. Okada,<sup>1</sup> and Y. Yamanaka<sup>1,8</sup>

Received 26 October 2011; revised 30 April 2012; accepted 7 May 2012; published 26 June 2012.

[1] To investigate the iron cycle at Station A4 in the Oyashio region of the western subarctic Pacific, we developed a 1-D ecosystem model consisting of 14 components including the iron cycle. The parameters associated with the iron cycle were optimized by assimilating monthly averaged data from time series observations for depth-integrated net primary production, nitrate, silicate, dissolved and particulate iron within the surface mixed layer (ML) and at two depths (200 and 300 m depth). The model successfully reproduced the observations and demonstrated that (1) on an annual basis, winter mixing of subsurface water supplies more dissolved iron ( $Fe_d$ ) to the ML than does dust dissolution, (2)  $Fe_d$  concentration in the ML rapidly declines to near-depletion during the peak period of the diatom bloom in spring, which results in an increasing consumption ratio of silicate to nitrogenous nutrients by diatoms as they become more iron-limited, causing a more rapid decrease of silicate compared to that of nitrogenous nutrients in the ML, followed by the silicate limitation of diatoms, and (3)  $Fe_d$  supplied to the ML by dust dissolution and desorption from particulate iron, by alleviating iron limitation of phytoplankton, supports their continuous utilization of nitrate from spring to fall even though  $Fe_d$  concentration in the ML remains low after the peak spring bloom. The model explained quantitatively the above behavior of  $Fe_d$  and other nutrients associated with  $Fe_d$  over the annual cycle in the Oyashio region.

**Citation:** Shigemitsu, M., T. Okunishi, J. Nishioka, H. Sumata, T. Hashioka, M. N. Aita, S. L. Smith, N. Yoshie, N. Okada, and Y. Yamanaka (2012), Development of a one-dimensional ecosystem model including the iron cycle applied to the Oyashio region, western subarctic Pacific, *J. Geophys. Res.*, *117*, C06021, doi:10.1029/2011JC007689.

### 1. Introduction

[2] Iron has been found to be a key element for limiting biological production in the high nitrate, low chlorophyll (HNLC) regions of the modern ocean [e.g., Tsuda *et al.*, 2003], and it has been thought that iron might have a large influence on biological production in the HNLC regions during glacial times [e.g., Martin *et al.*, 1989]. In addition, iron can also limit production of marine dinitrogen-fixers [e.g., Mills *et al.*, 2004] which can transform atmospheric molecular nitrogen into a bio-available form, fueling biological production, and affect nutrient cycles in the ocean. Thus, it is important for us to consider the iron flux in the ocean if we investigate fluxes of carbon and nutrients there.

[3] In this context, several biogeochemical modeling studies have recently incorporated the iron cycle into their marine ecosystem models [e.g., Aumont and Bopp, 2006; Moore *et al.*, 2004; Moore and Braucher, 2008] in order to clarify the relationships among carbon, nutrients and iron fluxes, and to reveal the cycle of iron itself in the ocean. These approaches are promising for investigating the fluxes of such bioelements because iron is likely to be the primary limiting nutrient for biological productivity in large parts of the ocean [e.g., Moore *et al.*, 2004]. However, observational data of iron needed to constrain such models are scarce, and there are few time series data sets available even locally.

<sup>1</sup>Faculty of Environmental Earth Science, Hokkaido University, Sapporo, Japan.

<sup>2</sup>National Research Institute of Fisheries Science, Fisheries Research Agency, Yokohama, Japan.

Corresponding author: M. Shigemitsu, Faculty of Environmental Earth Science, Hokkaido University, Kita-10, Nishi-5, Kita-Ku, Sapporo 060-0810, Japan. (ma-shige@ees.hokudai.ac.jp; Tel.: +81 117062288; Fax: +81 117064865)

©2012. American Geophysical Union. All Rights Reserved.  
10.1029/2011JC007689

<sup>3</sup>Pan-Okhotsk Research Center, Institute of Low Temperature Science, Hokkaido University, Sapporo, Japan.

<sup>4</sup>Alfred Wegener Institute for Polar and Marine Research, Bremerhaven, Germany.

<sup>5</sup>Japan Agency Marine-Earth Science and Technology, Yokohama, Japan.

<sup>6</sup>Graduate School of Fisheries Science, Hokkaido University, Sapporo, Japan.

<sup>7</sup>Center for Marine Environmental Studies, Ehime University, Matsuyama, Japan.

<sup>8</sup>Core Research for Evolutional Science and Technology, Japan Science and Technology Agency, Yokohama, Japan.

Previous modeling studies have only validated their iron cycles in the upper ocean by using data which are probably biased by limited coverage; i.e., under-sampling of some seasons. Time series observations which capture the full seasonal cycles over multiple years are needed to properly constrain the modeled iron cycle in the upper ocean. *Nishioka et al.* [2011] have recently reported the seasonal variations of dissolved iron in the mixed layer of the Oyashio region, western subarctic Pacific over several years. These data sets are valuable for constraining ecosystem models including the iron cycle. In addition, the data has indicated novel insights into a better understanding of the iron cycle in the upper ocean as follows: (1) Oceanic iron supply probably contributes as much as dust deposition to the dissolved iron in the upper ocean in the annual cycle, and (2) nitrate in the upper ocean continues to decrease from spring to fall despite the low dissolved iron concentration during summer and fall. The former is mostly clear from the observations, but it is difficult to quantitatively separate and understand each source and sink of dissolved iron in the upper ocean by using only observations. For the latter, it is also difficult to evaluate the factors controlling the processes by using only observational data. In addition, we don't have any information about the role of particulate iron in the oceanic biological production. Therefore, it is desirable to develop an ecosystem model including the iron cycle to quantitatively and globally analyze the presently available data and obtain some insights.

[4] In this study, as a first step, we aimed at developing an ecosystem model which explicitly describes dissolved and particulate iron, using a time series data set to constrain the relevant parameters, and thus to clarify details of the iron cycle in the Oyashio region. Here, we used the previously developed biogeochemical model, called NEMURO [e.g., *Yamanaka et al.*, 2004; *Fujii et al.*, 2007; *Kishi et al.*, 2007], as a platform because this model has (1) been applied over a wide range of the North Pacific including the Oyashio region, (2) succeeded in reproducing the biogeochemical characteristics there in the upper ocean [e.g., *Yamanaka et al.*, 2004; *Fujii et al.*, 2007], and (3) been embedded in a global ocean general circulation model (OGCM) [*Aita et al.*, 2007; *Sumata et al.*, 2010]. Extending the original model, we have developed a one-dimensional ecosystem model with nitrogen, silicon and iron cycles as a preliminary version of an ecosystem model which is later to be coupled with an OGCM. The model describes iron limitation of biological production. We have applied the model to Station A4 in the Oyashio region of the western subarctic Pacific, and investigated how the dissolved and particulate iron in the upper ocean is seasonally controlled and affects the biological production, in parallel with evaluating the model performance.

## 2. Data and Methods

### 2.1. Data

[5] We mainly used the time series data of dissolved iron, nitrate and chlorophyll *a* concentrations averaged within the surface mixed layer (ML), and surface mixed layer depth (MLD) during the period from 2003 to 2008 reported by *Nishioka et al.* [2011] at the station A4 (Figure 1). These data were obtained at a repeat hydrographic observation line called the A-line which Hokkaido National Fisheries

Research Institute (HNFRI) maintains in the Oyashio region [e.g., *Saito et al.*, 2002]. In addition to the *Nishioka et al.*'s [2011] data, we also used the time series nitrate, silicate and sigma-theta ( $\sigma_\theta$ ) data during the period from 1990 to 2007 obtained at HNFRI (A-line data home page, <http://hnf.fra.affrac.go.jp/a-line>) to complement the scarceness of the data within the ML and utilize data for nitrate and silicate obtained at 200 and 300 m depths in every month except for February. Moreover, we used three months' data of dissolved iron (January, April, and December) and one month's data of particulate iron (April) obtained at 200 and 300 m depths from 2003 to 2006 by *Nishioka et al.* [2007] and *Nishioka et al.* [2011], and depth-integrated net primary production data obtained in the Oyashio region from 1999 to 2002 [*Yokouchi et al.*, 2007]. MLD except for the data reported by *Nishioka et al.* [2011] is calculated as the depth at which  $\sigma_\theta$  changes by 0.125 from the surface value [*Levitus*, 1982]. The above data are used to constrain the parameters related to the iron cycle in the ecosystem model developed in this study. Note that for the silicate concentration in the ML, we used the data obtained during the period when the dissolved iron and nitrate data were obtained by *Nishioka et al.* [2011], because we wanted to focus on the relationships among nitrate, silicate and dissolved iron in the upper ocean. Note also that we omitted one sample having particulate iron concentration greater than 15 nM [*Nishioka et al.*, 2007] which was obtained from water with temperature lower than 2°C and salinity lower than 33.0 in May 2003, because characteristics of that water mass indicated that it was Coastal Oyashio water which differs from typical Oyashio water [*Ohtani*, 1989].

### 2.2. The Nitrogen, Silicon and Iron Regulated Marine Ecosystem Model (NSI-MEM)

[6] We developed a model to describe the nitrogen, silicon and iron regulated photosynthesis, based on the marine ecosystem model [*Yamanaka et al.*, 2004; *Fujii et al.*, 2007] which is basically the same as the North Pacific Ecosystem Model Used for Regional Oceanography (NEMURO) [*Kishi et al.*, 2007]. In brief, this ecosystem model includes two phytoplankton functional groups (non-diatom small phytoplankton (PS) and diatoms (PL)), three zooplankton functional groups (micro-(ZS), meso-(ZL) and predatory zooplankton (ZP)), nitrate ( $\text{NO}_3^-$ ), silicate ( $\text{Si}(\text{OH})_4$ ), ammonium ( $\text{NH}_4^+$ ), dissolved organic nitrogen (DON), detrital nitrogen (PON) and biogenic silica (Opal). The model also includes the carbon cycle, but we do not discuss the carbon cycle as it does not affect the model ecosystem behavior since carbon is not limitation factor. We extended the model as follows:

[7] 1. Iron cycle is formulated in the model mainly based on the parameterization used in *Moore et al.* [2004] and *Moore and Braucher* [2008]. We considered two components, dissolved iron ( $\text{Fe}_d$ ) and particulate iron ( $\text{Fe}_p$ ).

[8] 2. The original equation to describe the uptake of nutrients (Michaelis-Menten (MM) equation) is replaced, and the physiologically more consistent optimal uptake (OU) kinetics formulation proposed by *Smith and Yamanaka* [2007] and *Smith et al.* [2009] is adopted to apply the model globally in the near future. The most important feature of OU kinetics is that it represents the differing nutrient uptake response of plankton acclimated (or adapted by evolution) to different ambient nutrient concentrations. When applied, as

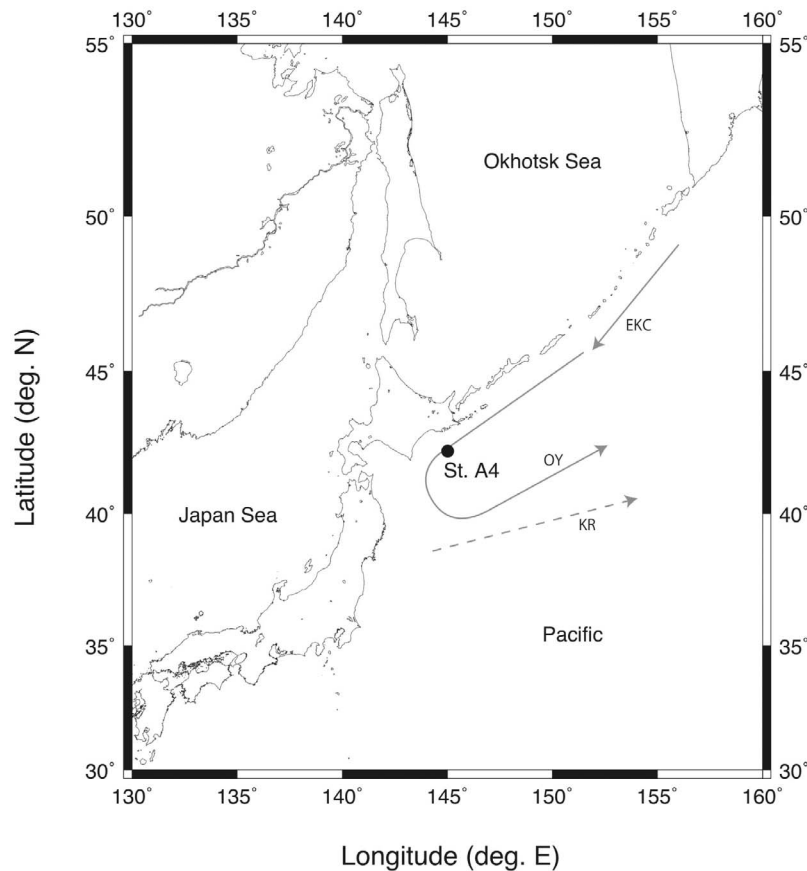


**Figure 1.** Map showing the location (Station A4) where the model developed in this study is applied. Arrows indicate a schematic image of surface water currents, and solid lines represent cold currents and dashed line the warm current. OY = Oyashio; EKC = East Kamchatka Current; KR = Kuroshio. Time series dissolved iron data of *Nishioka et al.* [2007] and *Nishioka et al.* [2011] used in this study were obtained at the Station A4.

in this study, at time scales longer than the time required for physiological acclimation, this results in a somewhat flatter shape of the uptake-versus-concentration response curve [Smith *et al.*, 2009], compared to MM kinetics. It also naturally separates the two fundamental traits of affinity (initial slope) and maximum uptake rate, which respectively characterize competitive ability at low versus high nutrient concentrations. The latter has advantages for tuning models and interpreting observations [Smith, 2011].

[9] 3. PON is divided into two classes, small (PON<sub>S</sub>) and large (PON<sub>L</sub>), which have different settling velocities. The aggregation processes among PON<sub>S</sub>, PON<sub>L</sub> and DON are also considered as in *Aumont and Bopp* [2006].

[10] 4. The Wroblewski-type ammonium inhibition for nitrate uptake by phytoplankton is replaced with the more consistent one of *Vallina and Le Quéré* [2008].

[11] 5. The Steele-type light dependency of phytoplankton photosynthesis [Steele, 1962] is replaced by that proposed by *Platt et al.* [1980] as in *Fujii et al.* [2007].

[12] 6. The vertical migration of ZL in the model is not considered as in *Sumata et al.* [2010] to allow the model to be applied globally.

[13] The structure of the ecosystem model is illustrated in Figure 2, and the model equations are presented in detail in Appendix A.

[14] The vertical distribution of each model compartment is simulated as a function of time using vertical diffusivities obtained from the OGCM run. Vertical advection and horizontal fluxes resulting from a divergent vertical flow field are not considered as in the previous modeling research in this region [Yamanaka *et al.*, 2004]. The governing equation can be formulated as follows:

$$\frac{\partial C_i}{\partial t} = -w_i \frac{\partial C_i}{\partial z} + \frac{\partial}{\partial z} \left( A_{HV} \frac{\partial C_i}{\partial z} \right) + SMS(C_i), \quad (1)$$

where  $A_{HV}$  is the vertical diffusive mixing coefficient and  $w_i$  is the sinking velocity which is nonzero for PON<sub>S</sub>, PON<sub>L</sub>, Opal and Fe<sub>p</sub>. The third term of the right-hand side is source minus sink (SMS) term due to the inherent biogeochemical processes.

[15] We will implement the ecosystem model within an OGCM in the future, in which case the physical environment will be obtained from the OGCM runs, as above. The OGCM output is identical to the one used by *Sumata et al.* [2010]. The horizontal resolution of the OGCM allows for mesoscale variability (“eddy permitting”) with a meridional grid of 0.1875° and a zonal grid spacing of 0.28125°. The water column is partitioned into 51 levels with the first 12 levels resolving the upper 120 m. In this study, we focus on the

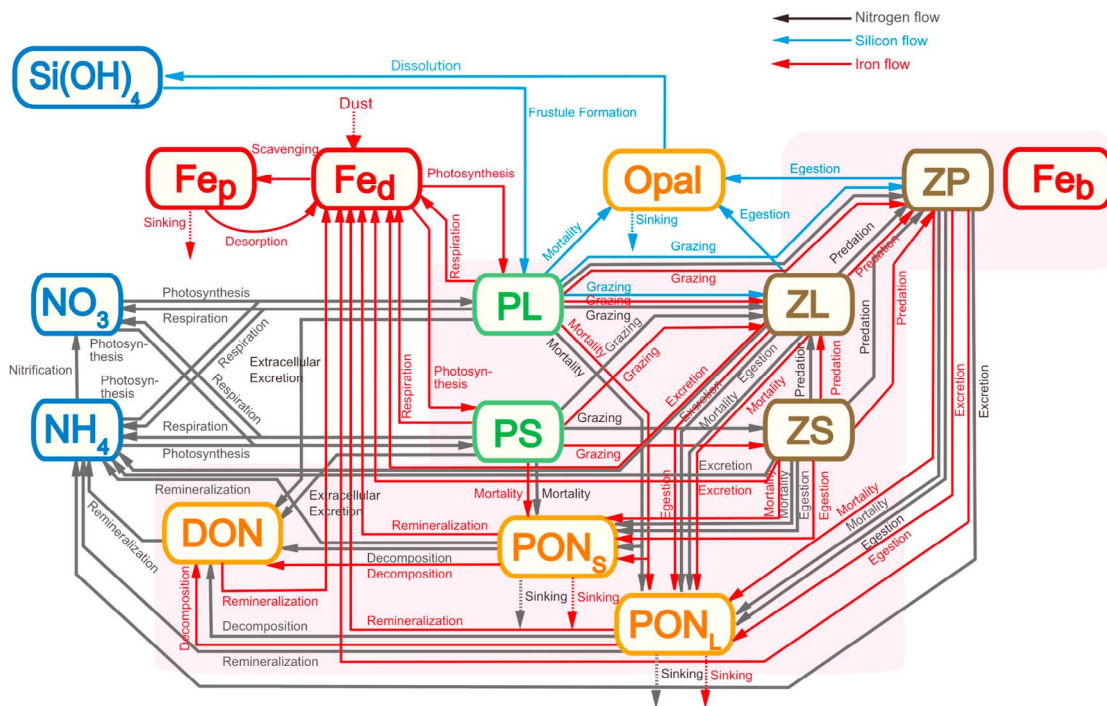


**Figure 2.** Schematic diagram of the ecosystem model.

effect of iron on the surface ocean biogeochemistry, and the upper 26 grids (about 500 m) were used. Data for water temperature, turbulent diffusivity, frequency of convective adjustment occurrence and light intensity were obtained from the OGCM hindcast experiment from 1990 to 2004 [Sumata *et al.*, 2010]. The frequency of convective adjustment occurrence is converted to the vertical diffusion coefficient as in Sumata *et al.* [2010]. The period from 1990 to 2004 is mostly consistent with the duration that the observational data are available. As for the dust data, we used the ensemble mean of 10 simulations during the same period as above of 20th century climate simulations with data assimilation carried out with the model called “Model for Interdisciplinary Research On Climate 3.2 (MIROC3.2)” [Mochizuki *et al.*, 2010]. From these data, we calculated each climatological forcing during the period from 1990 to 2004, and used that for the model run. The spin-up time is 8 years and the next 1 year’s results are shown in this study. The initial conditions for nitrate, silicate, and dissolved and particulate iron are from the observational data obtained in January 2003 by Nishioka *et al.* [2007] and HNFRI. Ammonium, Opal and DON are set at  $0.1 \mu\text{mol N l}^{-1}$ ,  $0.1 \mu\text{mol Si l}^{-1}$ , and  $0.1 \mu\text{mol N l}^{-1}$ , respectively. All types of plankton above and below 315 m depth are set to  $0.1 \mu\text{mol N l}^{-1}$  and  $0 \mu\text{mol N l}^{-1}$ , respectively, and both of PON are set to  $0.05 \mu\text{mol l}^{-1}$ . The boundary conditions at the bottom of the model domain for nitrate, silicate and dissolved and particulate iron are set at the same observations as the initial conditions, whereas no vertical gradients exist for other compartments at the bottom.

### 2.3. Optimization of Parameters Associated With the Iron Cycle

[16] The most important extension of the base model in this research is implementing the iron cycle. The parameters

associated with the iron cycle in the model can have wide ranges and are difficult to constrain. Because the base model has already been found to be able to reproduce the surface biogeochemistry in the western subarctic Pacific [e.g., Yamanaka *et al.*, 2004; Fujii *et al.*, 2007], we considered that we basically concentrate on optimizing the parameters related to the iron cycle in the model within the previously reported ranges by fitting the modeled results of nitrate, silicate and dissolved and particulate iron concentrations in ML and below the depth (200 and 300 m), and net primary production to the corresponding observations. In this study, we employed a micro-genetic algorithm as the optimization routine [Krishnakumar, 1989]. This algorithm has already been adopted and confirmed to work well in data assimilation studies in the field of marine science [e.g., Schartau and Oeschlies, 2003]. The prescribed upper and lower bounds of each parameter to be optimized, and the resolution used by the optimization to generate random samples in parameter space are shown in Table 1. In carrying out the optimization procedure, we defined the following cost function:

$$\text{Cost} = \sum_i^I \sum_k^K \frac{1}{N_{ik}} \sum_j \frac{1}{\sigma_i} (m_{ikj} - d_{ikj})^2, \quad (2)$$

where  $m_i$  is the modeled monthly mean of each type  $i$ , and  $d_i$  is the monthly “climatological” data of type  $i$  observation. The total number of observational data types,  $I$ , is 5 (nitrate, silicate, dissolved and particulate iron, and depth-integrated NPP). The index  $k$  represents the depths for which each observation is available and  $K$  is 3 (1: in the mixed layer (as for NPP, in the whole water column), 2: 200 m, 3: 300 m). The index  $j$  denotes the number of months ( $N_{ik}$ ) for which there exist observations of type  $i$  at depth  $k$ . We set the

**Table 1.** Setting of Model Parameters for Optimization and Optimal Estimates<sup>a</sup>

Parameter	Lower/Upper Bounds	Increment	Number of Possibilities	Optimal Estimates
$V_{0,PS}$	0.1/3.2	0.1	32	$0.6 \pm 0.3$
$A_{0,NO_3,PS}$	1/512	1	512	$282 \pm 112$
$V_{0,PL}$	0.1/3.2	0.1	32	$0.8 \pm 0.5$
$A_{0,NO_3,PL}$	1/512	1	512	$252 \pm 115$
$w_{PONI}^{min}, w_{PONI}^{Opal}$	3/48	3.0	16	$6 \pm 3$
$w_{PONI}^{min}, w_{PONI}^{Opal}$	48/198	10.0	16	$198 \pm 69$
$V_{PDOS}, V_{PAOS}, V_{PDOL}, V_{PAOL}$	0.01/0.32	0.01	32	$0.08 \pm 0.06$
$V_{DAO}$	0.01/0.32	0.01	32	$0.15 \pm 0.14$
$V_{Opal}$	0.01/0.32	0.01	32	$0.16 \pm 0.12$
$R_{FeN}$	$1.0 \times 10^{-5}/7.3 \times 10^{-5}$	$0.1 \times 10^{-5}$	64	$1.7 \times 10^{-5} \pm 2.6 \times 10^{-5}$
$R_{SiNL}$	1.7/4.8	0.1	32	$3.6 \pm 0.9$
$R_{SiNH}$	1.0/1.7	0.1	8	$1.0 \pm 0.0$
$Fe_{SiN}^*$	0.01/0.63	0.02	32	$0.03 \pm 0.35$
$\alpha$	1.0/4.5	0.5	8	$4.0 \pm 1.6$
$\lambda_{desorption}$	0.001/0.128	0.001	128	$0.003 \pm 0.002$
$\lambda_{scav}$	0.001/0.256	0.001	256	$0.185 \pm 0.084$
$\gamma_{high}$	0.0001/0.0256	0.0002	128	$0.0044 \pm 0.0044$
$w_{Fep}$	0.001/0.128	0.001	128	$0.001 \pm 0.006$
$f_{Fep}$	0.3/1.0	0.1	8	$1.0 \pm 0.0$

<sup>a</sup>Each parameter is represented by a discrete binary string of a certain length. One individual combines all strings of all parameters (one parameter set). The number of possibilities expresses the number of binary digits that describes the number of possible values within the prescribed upper and lower bounds for parameter variations.

maximum depth for data to be assimilated into the model at 300 m. The same weight is put on each type observation at each depth by dividing by the number of available observations of each type at each depth ( $N_{ik}$ ). The assigned weights for nitrate and silicate are  $\sigma_{nitrate} = 0.1 \mu\text{mol l}^{-1}$  and  $\sigma_{silicate} = 0.1 \mu\text{mol l}^{-1}$ . For dissolved and particulate iron, weights of  $\sigma_{Fed} = 0.005 \text{ nmol l}^{-1}$  and  $\sigma_{Fep} = 0.1 \text{ nmol l}^{-1}$  are assumed. For net primary production,  $\sigma_{NPP}$  is set at  $8 \text{ mg C m}^{-2} \text{ d}^{-1}$ . In the model, the maximum potential growth rate of PL ( $V_{0,PL}$ ) is assumed to be larger than the one of PS ( $V_{0,PS}$ ), and the maximum potential affinity for nitrate of PL ( $A_{0,NO_3,PL}$ ) is assumed to be lower than that of PS ( $A_{0,NO_3,PS}$ ) (detailed in Appendix A for  $V_0$  and  $A_0$ ) based on both the fact that diatom spring bloom occurs in the Oyashio region every year and from spring to fall other small phytoplankton increases [e.g., Saito *et al.*, 2002], and the previous model results [Yamanaka *et al.*, 2004]. However, the assumptions could not be realized by the presently available observational data in the preliminary optimizations. Thus, we determined to add the following penalty function to the above cost function if the case is not met in the optimization procedure:

$$J^{penal} = \frac{1}{\sigma_A^2} (|A_{0,NO_3,PS} - A_{0,NO_3,PL}| - (A_{0,NO_3,PS} - A_{0,NO_3,PL}))^2 + \frac{1}{\sigma_V^2} (|V_{0,PL} - V_{0,PS}| - (V_{0,PL} - V_{0,PS}))^2, \quad (3)$$

$J^{penal}$  is zero if the above conditions are met. Arbitrarily, we set the  $\sigma_A$  and  $\sigma_V$  at  $86400 \text{ l molN}^{-1} \text{ day}^{-1}$  and  $0.0001 \text{ day}^{-1}$ . These parameters should be constrained by the other observational data (e.g., size-fractionated Chlorophyll *a*) in the future. We also estimated the errors of the parameters optimized using the method of Schartau and Oeschlies [2003]. Briefly, Gaussian noise, having a variance ( $\sigma_i^2$ ) identical to that prescribed for each observation in the cost function, was added to the observed data. We performed 5 optimizations, and from the estimated parameter values, each parameter

error was calculated as in Schartau and Oeschlies [2003] (Table 1). In all cases, the minimum cost function was identified after 38,000 iterations (19 individuals times 2000 generations).

### 3. Results

#### 3.1. Comparison of Simulated Results With Observations

[17] The physical forcing used here agrees well with the observations (Figure 3). The modeled mixed layer depth (MLD) defined as the diffusivity of  $1.0 \times 10^{-4} \text{ m}^2 \text{ s}^{-1}$  is in good agreement with the observations obtained during the period from 1990 to 2007. The water temperature averaged in ML also agrees well with the observations. As far as we know, there are no seasonal observations of aeolian dust at this study site. However, in the northern part of Japan, the seasonal cycle of dust has been observed, indicating a dust flux maximum in spring, such as April or May [e.g., Uematsu *et al.*, 2003], whereas dust flux forcing herein has a maximum in fall (Figure 3). The difference between the dust flux used in this study and the observation might be a result of a bias in the model from which the forcing was obtained. However, the annual supply of dust estimated from the seawater aluminum concentration by Measures *et al.* [2005] (about  $0.3 \text{ g m}^{-2} \text{ year}^{-1}$ ) seems to be in good agreement with the model forcing of annually integrated dust load (about  $0.3 \text{ g m}^{-2} \text{ year}^{-1}$ ). To check to see if the difference in seasonal cycle of dust flux between with the maximum in spring and fall is important for the modeled results, we conducted an additional simulation using dust forcing having a maximum in spring, with the same annual load of dust as our standard dust flux (Figure 3). In this experiment, we found that the important modeled properties, such as net primary production, nutrients, dissolved and particulate iron in ML were quite insensitive to the timing of seasonal peak of the dust deposition, at least for the present experimental

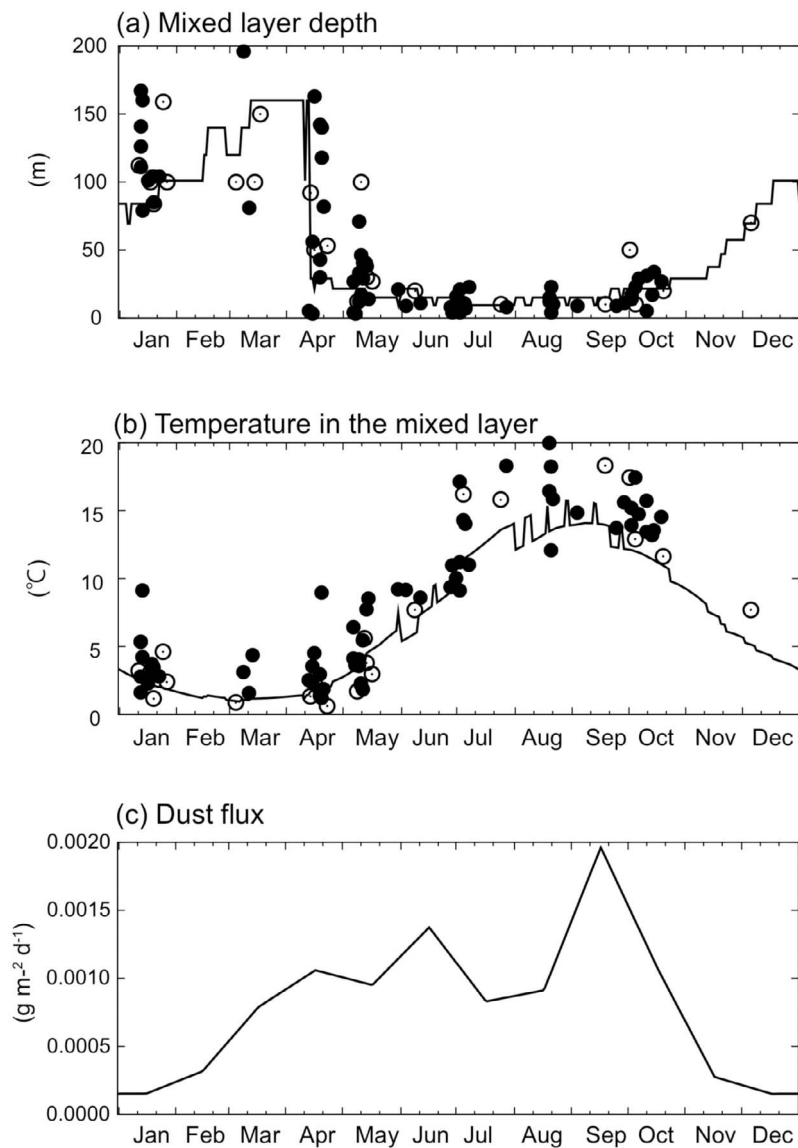


**Figure 3.** Physical forcing used when running the ecosystem model. (a) Mixed layer depth (m) (defined as the depth at which the modeled vertical diffusive coefficient is  $1.0 \times 10^{-4} \text{ m}^2 \text{ s}^{-1}$ ), (b) temperature averaged in the mixed layer ( $^{\circ}\text{C}$ ), and (c) dust flux ( $\text{g m}^{-2} \text{ d}^{-1}$ ). Symbols represent the observational data (open circles, *Nishioka et al.* [2011]; solid circles, HNFRI data). Note that the mixed layer depth on March 14, 1998 is deeper than 300 m depth and out of range of Figure 3a.

design (Figure B1). From these results, we consider that there is no problem to optimize the parameters related to the iron cycle in the model with the original dust forcing.

[18] The simulated results with the prescribed physical forcing are shown in Figure 4. All the biogeochemical components are well reproduced by the model. This indicates that the parameter optimization worked well. Nutrient-rich water in the lower layer is supplied to the surface by the enhanced mixing in winter (Figure 3), and simulated nitrate, silicate and dissolved iron concentrations are highest in early spring. The simulated high surface nutrients concentrations, stratification of the surface waters and increased solar radiation trigger a diatom spring bloom as seen in NPP and diatom (PL) biomass in ML followed by sharp decline to July. After

the peak spring bloom of PL, non-diatom small phytoplankton (PS), which does not need silicate for its growth, continues to increase and shows maxima of its production and biomass in June despite low concentrations of nutrients. In the period, remineralization and decomposition of debris of PL temporarily supply nutrients to the ML (Figure 4), which alleviates nutrients limitation of PS to some extent (Figure 5). Alleviated nutrients limitation of PS combines with rising temperature and light intensity to produce transient peaks of PS production and biomass. As nutrient consumption by phytoplankton proceeds from spring to fall, nitrate concentration in ML decreases to near-depletion while silicate and dissolved iron concentrations rapidly decline during the peak period of PL biomass and gradually rise with the decrease of

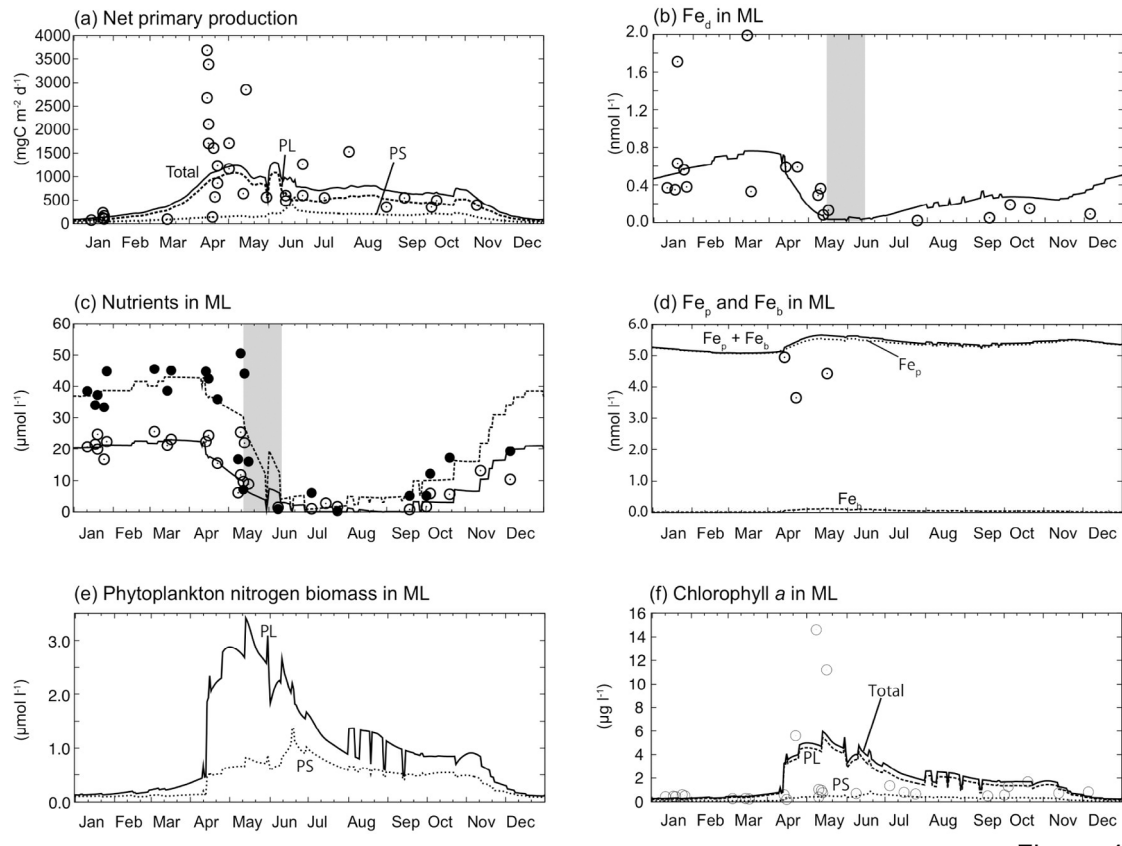


**Figure 4.** Simulated results of (a) net primary production, (b) dissolved iron ( $Fe_d$ ) averaged in the mixed layer (ML), (c) nutrients, nitrate (solid line) and silicate (dashed line), averaged in ML, (d) total particulate iron ( $Fe_p + Fe_b$ ; solid line), particulate iron ( $Fe_p$ ; dotted line) and biological iron ( $Fe_b$ ; dashed line) averaged in ML, (e) phytoplankton biomass (PL, solid line; PS, dotted line) averaged in ML, and (f) chlorophyll *a* concentration of PS (dotted line), PL (dashed line) and their total (solid line) averaged in ML. Symbols represent the corresponding observational data [Yokouchi *et al.*, 2007; Nishioka *et al.*, 2011]. In Figure 4c, solid (open) circles represent the observed silicate (nitrate) averaged over ML. In Figure 4f, a fixed C/Chl-*a* ratio of 125 and 50 for PS and PL, respectively, were used to estimate modeled chlorophyll *a* concentration as in Sumata *et al.* [2010]. Shaded areas in Figures 4b and 4c represent the period when the stoichiometry of silicon to nitrogen of diatom (PL) shifted from  $R_{SiNH}$  to  $R_{SiNL}$  (see Table A1 and equation (A68)).

PL biomass. On the other hand, the modeled particulate iron concentration is not more variable compared to the other components. The modeled particulate iron does not directly correspond to the observed particulate iron but the sum of the modeled particulate iron ( $Fe_p$ ) and biological iron ( $Fe_b$ ). The contribution of  $Fe_b$  to the total is small. The sum of modeled  $Fe_p$  plus  $Fe_b$  in ML is a little higher than observed in a few cases. Along with the decrease of nitrate concentration in ML toward fall, simulated NPP and biomass of PL decrease more than those of PS because of silicate limitation which follows iron limitation as explained in section 4.1. From fall to winter, MLD again begins to deepen, solar radiation decreases, and as a result NPP and biomass also decline. That results in the increases of simulated nitrate, silicate and dissolved iron concentrations. Again, the model well reproduced the characteristic nutrient behavior in ML seen in the observations that nitrate is exhausted from spring to fall when the dissolved iron concentration is low while silicate is not depleted.

Finally, we compared the modeled chlorophyll *a* concentration with the observations, which the model reproduced well, even though the observed chlorophyll *a* concentration was not used in the parameter optimization. This reveals that assimilated data are sufficient, and the model formulation is adequate to produce substantially robust results, at least for chlorophyll *a*. In the future, when embedding this ecosystem model in the OGCM, we will further investigate its robustness.

### 3.2. Optimized Parameters Related to the Iron Cycle in the Model

[19] The optimization results for parameters related to the iron cycle in the model are summarized in Table 1. Most parameters except for the maximum sinking velocity of  $PON_L$  and Opal ( $w_{max}^{PON_L}$ ,  $w_{max}^{Opal}$ ), PL stoichiometry of silicate to nitrogenous nutrients uptake in iron-replete condition ( $R_{SiNH}$ ),  $Fe_p$  sinking velocity ( $w_{Fe_p}$ ), and fraction of  $Fe_p$  which is not removed from the model domain just after being

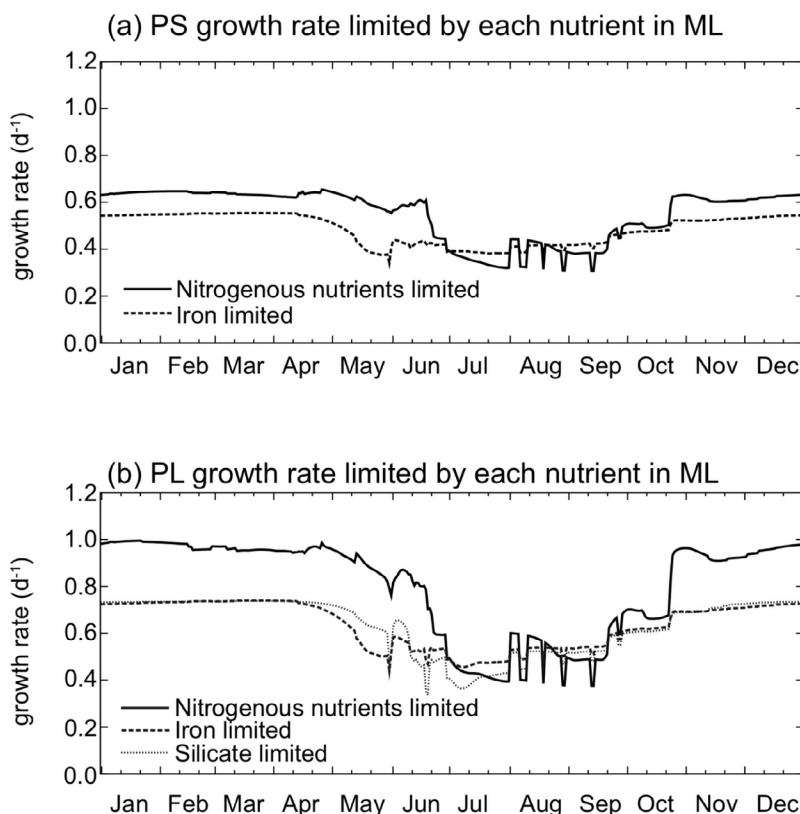


**Figure 5.** Modeled phytoplankton growth rate limited by each nutrients for (a) PS (non-diatom small phytoplankton) and (b) PL (diatoms) averaged within the mixed layer (ML). Note that the growth rate here represents the rate where limitation by light and temperature is not considered.

converted from  $Fe_d$  to  $Fe_p$  during the scavenging process (i.e., in this model, some fraction of  $Fe_p$  just after being produced is instantaneously removed from the model domain to prevent Fe from accumulating continuously in the model domain) ( $f_{Fe_p}$ ) are well constrained within the prescribed ranges. The above four parameters are estimated at the prescribed upper or lower boundary values. Implications of the optimized parameter values are discussed in section 4.3.

## 4. Discussion

### 4.1. Iron Limitation for Phytoplankton Growth in the Model

[20] A major reason for incorporating the iron cycle in an ecosystem model is being able to express the iron limitation of phytoplankton growth. The modeled phytoplankton growth rate limited by each nutrient (nitrate plus ammonium, silicate, and dissolved iron) is shown in Figure 5. For non-diatom small phytoplankton (PS), model results indicate the stronger limitation on PS by dissolved iron than by nitrogenous nutrients over a year except for summer. In summer, PS growth is limited by nitrogenous nutrients. As for diatoms (PL), in winter to early spring, PL growth is limited by silicate or dissolved iron to the same extent as each other. During the peak period of the spring bloom, the growth rapidly begins to be limited by the dissolved iron followed by silicate. In the model, dissolved iron concentration in ML reaches the optimized threshold value of  $0.03 \text{ nmol l}^{-1}$

( $Fe_{SiN}^*$ ) for shift in PL stoichiometry of Si to N (Table 1 and Figures 4 and 5) during the peak spring bloom, which leads to rapid silicate depletion relative to nitrogenous nutrients and as a result silicate limitation. This is caused by the fact that the PL stoichiometry of Si to N is changed depending on the surrounding  $Fe_d$  concentration in the model (see Appendix A, equation (A68)). The process of the PL nutrient limitation shift from dissolved iron to silicate is the same as other modeling research [e.g., Lancelot *et al.*, 2000; Takeda *et al.*, 2006] which also predicted a shift in the nutrient limitation of diatoms from iron to silicate due to the imbalance between silicate and nitrogenous nutrients assimilation after an iron-replete condition in the Polar Front region of the Southern Ocean and the Northeastern subarctic Pacific. Saito *et al.* [2002] showed an increase in silicate to nitrate uptake ratio by phytoplankton during mid to late spring bloom in the Oyashio region. They suggested the increase of the uptake ratio might be due to light or Fe limitation on diatoms, for example, as indicated by Takeda [1998]. The model result is consistent with their observations in the same region. In July to September, PL are limited by nitrogenous nutrients as in PS. Saito *et al.* [2002] also reported that during spring to fall nitrate and silicate are consumed, and the former nutrient is exhausted while the latter is not completely consumed. The characteristics of nutrients behaviors are seen in the observed data used in this study (Figure 4) as stated in section 3.1, and those were well

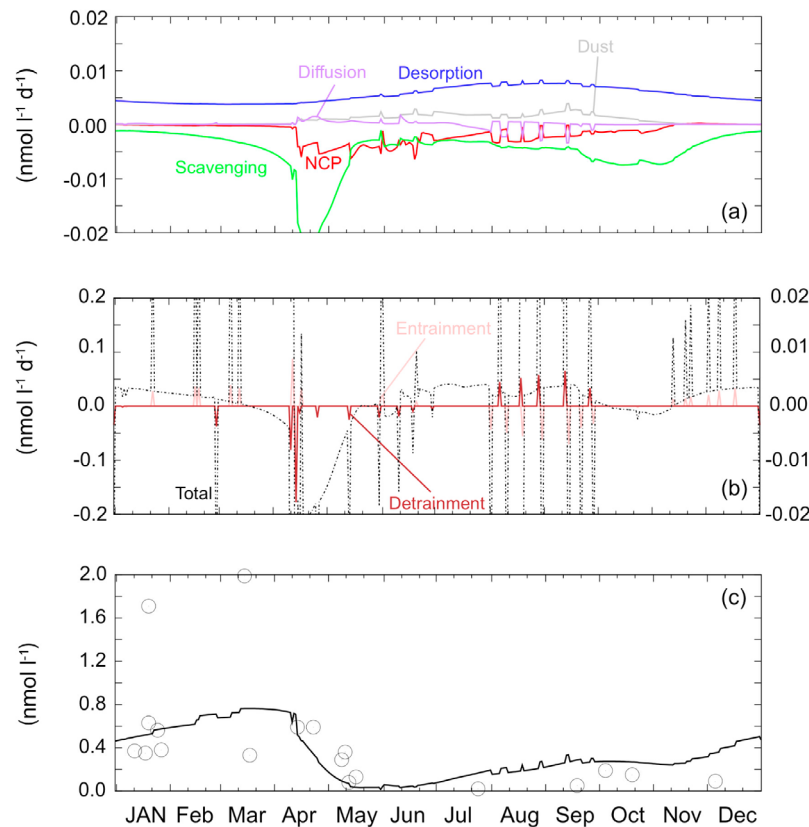


**Figure 6.** Modeled seasonal variation of (a) each source/sink term of dissolved iron ( $\text{Fe}_d$ ) within the mixed layer due to scavenging (green line), net community production (NCP) (red line), diffusion (purple line), desorption (blue line), and dust (gray line) and (b) that due to entrainment (pink line), detrainment (brown line), and total from each source/sink term (black dash-dotted line). (c) Simulated dissolved iron concentration in the mixed layer as in Figure 4b. In Figure 6b, the expanded scale on the right y axis is used for the total.

reproduced by the model. Thus, the result that the modeled phytoplankton growth in summer is limited by nitrogenous nutrients also seems to be reasonable.

#### 4.2. Controlling Factors of Seasonal Variation in Dissolved and Particulate Iron in the Model

[21] The characteristic seasonal variations of the modeled dissolved iron ( $\text{Fe}_d$ ) averaged in ML are as follows: (1) the maximum is reached in early spring, (2) rapid decrease from spring to early summer, and (3) gradual increase from summer to winter. On the other hand, the seasonal variation of the modeled particulate iron (the sum of the modeled particulate ( $\text{Fe}_p$ ) and biological iron ( $\text{Fe}_b$ )) averaged in ML are relatively constant, but the following can be seen: (1) the maximum is reached during the diatom spring bloom period, and (2) there is a decrease from the peak spring bloom period to winter. Here we examine the factors controlling these patterns in the model.

[22]  $\text{Fe}_d$  in ML in the model is controlled by various sources (dust dissolution, desorption from  $\text{Fe}_p$ , detrainment, entrainment, and diffusion) and sinks (scavenging to  $\text{Fe}_p$ , net community production (NCP), detrainment, entrainment and diffusion). As for entrainment, if entrainment of the water below ML with higher (lower) concentration of  $\text{Fe}_d$  compared

to that in ML occurs, the entrainment becomes source (sink) of  $\text{Fe}_d$  in ML. As for detrainment, that also sometimes affects  $\text{Fe}_d$  in ML when there is a slight concentration gradient of  $\text{Fe}_d$  at the base of ML. Thus, if the detrainment of the water at the bottom of ML with higher (lower) concentration of  $\text{Fe}_d$  compared to that above the bottom occurs, that becomes sink (source) of  $\text{Fe}_d$  in ML. The time rate of change of  $\text{Fe}_d$  concentration averaged in ML by each source/sink is shown in Figure 6. During the period from fall to winter, entrainment is the main source process and  $\text{Fe}_d$  concentration increases. In this period, the desorption from  $\text{Fe}_p$  is the second largest source of  $\text{Fe}_d$  although the rate is much smaller compared to the entrainment. In spring, scavenging is the largest sink process, and net community production (NCP) is the second largest one. The sum of them is exceeding other source processes in April to May, the peak diatom spring bloom (Figure 4), and  $\text{Fe}_d$  decreases rapidly. After the period, both desorption from  $\text{Fe}_p$  and dust dissolution as the source process are larger than other sink processes, and  $\text{Fe}_d$  gradually increases. Optimized solubility of iron in dust was 4% (Table 1) which was a little larger than the recent estimate based on the observations (1.2–2.3% [Ooki *et al.*, 2009]). In addition, the annual load of dust as the boundary condition at the surface of the model domain is similar to the observation estimated at

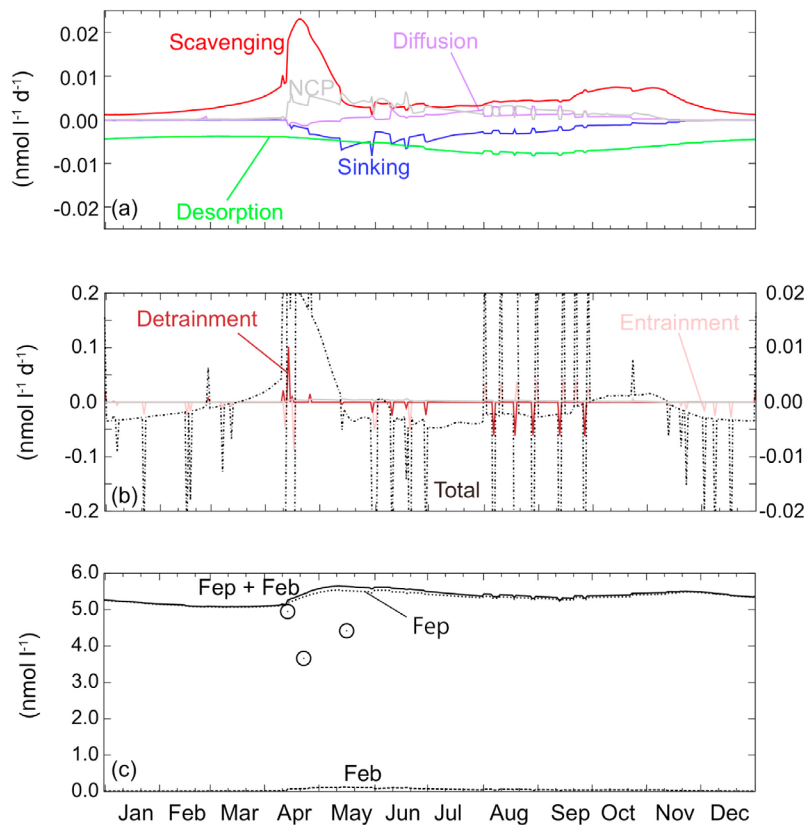


**Figure 7.** Modeled seasonal variation of (a) each source/sink term of total particulate iron ( $\text{Fe}_p + \text{Fe}_b$ ) within the mixed layer due to scavenging (red line), net community production (NCP) (gray line), diffusion (purple line), desorption (green line), and sinking (blue line) and (b) that due to entrainment (pink line), detrainment (brown line), and total from each source/sink term (black dash-dotted line). (c) Simulated particulate iron concentrations averaged within the mixed layer as in Figure 4d. In Figure 7b, the expanded scale on the right y axis is used for the total.

about  $0.3 \text{ g m}^{-2} \text{ year}^{-1}$  [Measures *et al.*, 2005] as explained above. Nevertheless, the dust dissolution does not contribute, to a great extent, to the time rate of change of  $\text{Fe}_d$  concentration. This result indicates that  $\text{Fe}_d$  in ML is supplied mainly by the entrainment in fall to winter. This model result corroborates the implication of Nishioka *et al.* [2011] that  $\text{Fe}_d$  source in ML of the Oyashio region is mainly vertical winter mixing, while in the future we must confirm the effect of horizontal transport because this one-dimensional model does not account for this process. Although dust dissolution does not seem to be the main source process of  $\text{Fe}_d$  in ML at this study site, the model results show that the dust dissolution plays an important role during the period of nitrate exhaustion from June to September, together with the desorption from  $\text{Fe}_p$ . Those sources of  $\text{Fe}_d$ , to some extent, alleviate iron limitation on phytoplankton during the period (Figures 5 and 6), and as a result allow phytoplankton to consume nitrogenous nutrients to near depletion levels during this period as explained in section 4.1 and PL to keep the stoichiometry of Si to N uptake unity in iron-replete condition ( $R_{\text{SiNH}}$ ). Thus, nitrogenous nutrients continue to be utilized although  $\text{Fe}_d$  concentration in ML is not high, on the other hand silicate continues to be not consumed but gradually increased in the model. Note that (1) in spring to fall the entrainment and detrainment sporadically become source/sink processes for  $\text{Fe}_d$  because of the

reasons above, but they are almost canceled out, and (2) diffusion is the minor process for  $\text{Fe}_d$  in ML (Figure 6).

[23] For the modeled particulate iron in ML, as stated in section 3.1, that is a little higher than that observed in a few cases. This is because  $\sigma_{\text{Fep}}$  is set to a relatively high value due to the seasonal data not existing and the contribution to the cost function (equation (2)) is the smallest compared to other components. Although the limited availability of observations makes it difficult for us to properly evaluate whether or not the model reproduce the seasonal variation of particulate iron, examining modeled response in detail is important for understanding how the model behaves at present and how to improve it in the future. The observed particulate iron in ML probably corresponds to the sum of the modeled  $\text{Fe}_p$  and  $\text{Fe}_b$ . For the modeled total particulate iron ( $\text{Fe}_p$  plus  $\text{Fe}_b$ ) in ML, there are sources (scavenging, net community production (NCP), detrainment, entrainment and diffusion) and sinks (desorption, sinking, detrainment, entrainment and diffusion) processes. These terms are calculated and shown in Figure 7. For entrainment and detrainment, the same things as  $\text{Fe}_d$  apply to that for the total particulate iron. For the total particulate iron ( $\text{Fe}_p + \text{Fe}_b$ ), the maximum concentration in spring is affected mainly by the scavenging and NCP (Figure 7). From spring to fall, the sink processes of sinking and desorption are a little larger than the source processes of

scavenging, NCP and diffusion, and the total particulate iron decreases. From fall to winter, entrainment works as a sink process, and the total particulate iron declines more rapidly. In this period, the total particulate iron concentration below ML is lower than that in ML. Looking into the seasonal variation of the modeled total particulate iron in detail, the above sources and sinks seasonally affect the concentration in ML. However, roughly speaking, the concentration of the total particulate iron is relatively constant all year-round, which means that the budget as a result of the sum of all the rates of change does not contribute much to the concentration of the modeled total particulate iron in ML on the annual cycle (Figure 7). So far, the sinking of  $Fe_p$  is the smallest sink process almost over a year. The relatively constant concentration of the total particulate iron is mainly due to the very slow sinking velocity (Table 1). In addition, the optimized desorption rate of  $0.003 \text{ (d}^{-1}\text{)}$  is one order of magnitude smaller than the experimentally estimated value of  $0.03 \text{ (d}^{-1}\text{)}$  [Hurst and Bruland, 2007]. It is possible that this slow sinking velocity and low desorption rate might be spurious results of the 1-D model used in this study. If the true desorption rate is actually higher, the impact on the upper ocean  $Fe_d$  might be larger, although a faster sinking velocity of  $Fe_p$  might compensate for that effect. Nishioka et al. [2011] indicated that the enormous amount of  $Fe_d$  is laterally transported into the intermediate layer with  $26.6\text{--}27.5\sigma_\theta$  (about 100 to 1300 m depth) in the Oyashio region by using  $Fe^*$  (defined as the Fe supplied from an external source decoupled from the organic matter regeneration cycle). As stated in section 2.2, we set the model domain up to the depth of about 500 m because  $Fe^*$  peaks at St. A4 were seen at around 500 m depth and in the upper 200 m the value was near zero which means that the lateral transport of  $Fe_d$  around 500 m depth at St. A4 is large, but that in the upper ocean is, if anything, small. The lateral transport of  $Fe_d$  at around 500 m is represented in the model by the simulated  $Fe_d$  being restored to a constant observed value. However, particulate iron might be affected to some extent in the upper ocean by the lateral transport since in one vertical profile observed at St. A4, there is a maximum of that at around 100 m depth which the present model cannot reproduce (Figure 9; detailed in the next section). If particulate iron is affected by lateral transport in the upper ocean, low values of both sinking velocity and desorption rate of  $Fe_p$  will be necessary to maintain the observed high concentration of particulate iron (Figures 4 and 9) in this model because the particulate iron concentrations at 200 and 300 m depths are considered in the cost function (equation (2)). Particulate iron concentration must be high through the water column in the Oyashio region inferred from the data obtained at several stations except for St. A4 [Nishioka et al., 2007], but the available data at St. A4 are extremely few. Thus, for slow sinking and low desorption rates of  $Fe_p$ , we will have to carefully investigate whether or not the present sinking and desorption rates are valid when incorporating the model into the OGCM. The sinking and desorption rates are again detailed in the next section.

#### 4.3. Implication of Optimized Parameters Associated With Iron Cycle in the Model

[24] As shown in Table 1, we optimized 19 parameters associated with the iron cycle in the model by assimilating the

time series observational data of monthly averaged (1) depth-integrated net primary production, (2) nitrate, (3) silicate and both (4) dissolved and (5) particulate iron within ML and two depths (200 and 300 m depth).

[25] In the present model, we replaced the MM kinetics by OU kinetics (see Appendix A, equations (A15)–(A20) and (A23)–(A30)). Despite the optimization, there is room for improvement in the estimated values of potential maximum growth rate and affinity for nitrate. That is because these parameters are not constrained by the presently available observed data, and we imposed the penalty (equation (3)) on the cost function as stated in section 2.3. As detailed in Appendix A, potential maximum affinities of phytoplankton for nutrients other than nitrate are estimated from values of Michaelis-Menten half-saturation constants reported by previous modeling studies. This is simply because the available field observations are not sufficient to constrain all uptake parameters, which would be just as true for a model using Michaelis-Menten kinetics as for this model using OU kinetics. The optimized ratios of potential maximum growth rate ( $V_{0,PS}, V_{0,PL}$ ) to potential maximum affinity ( $A_{0,NO_3,PS}, A_{0,NO_3,PL}$ ) of phytoplankton uptake for nitrate,  $0.025 \text{ (}\mu\text{mol l}^{-1}\text{)}$  for PS and  $0.037 \text{ (}\mu\text{mol l}^{-1}\text{)}$  for PL, seem to be reasonable so far, although we will have to reconsider the values in the future. Those values are close to the lower limit of the previous estimates ( $0.047\text{--}0.14$ ; Smith, 2010), based on limited field data from the North Atlantic.

[26] For the minimum and maximum sinking velocities for  $PON_L$  ( $w_{min}^{PON_L}, w_{max}^{PON_L}$ ) and Opal ( $w_{min}^{Opal}, w_{max}^{Opal}$ ), the minimum sinking velocity in ML is estimated at  $6 \text{ m d}^{-1}$  and the maximum at 2000 m depth is estimated at  $198 \text{ m d}^{-1}$ . Although the data available for sinking velocities in the open ocean are poor, the observed sinking velocities in the upper part of the ocean and in the deep sea range from 10 to 50 and from 100 to 250  $\text{m d}^{-1}$ , respectively [e.g., Berelson, 2002]. Our estimate of the minimum sinking velocity is well constrained within the similar prescribed range to the previously reported one and seems to be reasonable. The estimated maximum sinking rate is at the upper limit of the prescribed range, and might need to be increased. Note that the sinking speed of the particles in the present model is not altered by the Opal, dust and calcium carbonate (not calculated in this study) contents in it (“The ballast effect” [Armstrong et al., 2002]), and Opal is assumed to sink at the same speed as  $PON_L$  (see Appendix A, equations (A73) and (A74)).

[27] As for the decomposition and remineralization rate ( $V_{PDOS}, V_{PAOS}, V_{PDOL}, V_{PAOL}$ ) at  $0^\circ\text{C}$  of  $PON_S$  and  $PON_L$ , we estimated that at  $0.08 \text{ day}^{-1}$  which is close to the previously used value of  $0.1 \text{ day}^{-1}$  in the Oyashio region [e.g., Yamanaka et al., 2004]. The remineralization rate of DON at  $0^\circ\text{C}$  ( $V_{DA0}$ ) ( $0.15 \text{ d}^{-1}$ ) and the dissolution rate of Opal to silicate ( $V_{Opal}$ ) ( $0.16 \text{ d}^{-1}$ ) are also similar to the previously used values of  $0.1 \text{ d}^{-1}$  [Yamanaka et al., 2004].

[28] The optimized stoichiometric ratio of iron to nitrogen in plankton ( $R_{FeN}$ ) is  $1.7 \times 10^{-5}$  and reasonable because it is close to the observation-based estimate,  $2.0 \times 10^{-5}$  which was calculated from the slope of the surface dissolved iron without one outlier versus nitrate plot during the dissolved iron decreasing period as in Nishioka et al. [2011].

[29] For the stoichiometric ratio of silicate to nitrogenous nutrients of diatoms in iron-rich and iron-deficient conditions

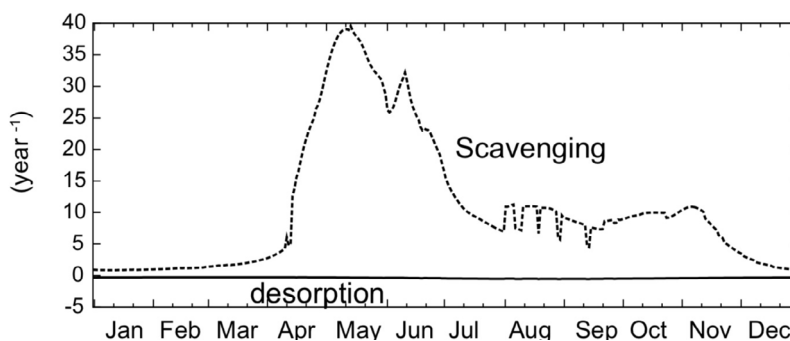


**Figure 8.** Simulated scavenging and desorption rate of iron averaged in the mixed layer.

( $R_{\text{SiNH}}$  and  $R_{\text{SiNL}}$ ), the optimized values of 1.0 for  $R_{\text{SiNH}}$  and 3.6 for  $R_{\text{SiNL}}$  appear to be reasonable values because the value of 1.0 uptake ratio for diatoms under iron-replete conditions are observed [e.g., *Scarratt et al.*, 2006; *Kudo et al.*, 2006] and the value of 3.6 for  $R_{\text{SiNL}}$  falls within the silicate to nitrate uptake ratios measured in low-iron HNLC waters in the Southern Ocean (1.3–8 [*Franck et al.*, 2000]) and in the eastern tropical Pacific (2.5–6.0 [*Franck et al.*, 2003]).

[30] The threshold value of dissolved iron ( $\text{Fe}_{\text{SiNH}}^*$ ; see equation (A68)) for the shift in  $R_{\text{SiNH}}$  to  $R_{\text{SiNL}}$  is  $0.03 \text{ nmol l}^{-1}$  and well constrained within the prescribed range. This leads to the model results that silicate is utilized by phytoplankton more rapidly than nitrate in  $\text{Fe}_d$  deficient period (Figure 4), and PL suffers from silicate limitation after the iron limitation during the peak period of the spring bloom in the model (Figure 5). As stated above, this phenomenon is reported by *Saito et al.* [2002] and the threshold value seems to be reasonable from the viewpoint of the way of drawdown of nutrients during the peak spring bloom and the succession of the limitation of nutrients on diatoms during and after the period, i.e., iron to silicate [e.g., *Takeda et al.*, 2006]. The physiological basis for the effect of iron on diatom silicon metabolism is poorly understood [*Martin-Jézéquel et al.*, 2000], and some other nutrient stress may be associated with the ratio shift [*Takeda et al.*, 2006]. Thus, the present parameterization for the ratio shift which is simply dependent on the dissolved iron concentration might have to be modified in the future.

[31] The solubility of airborne iron ( $\alpha$ ) is estimated at the value of 4.0%. This value is a little higher than the recent estimation of 1.2 to 2.3 [Ooki et al., 2009]. The annual dust load used in this study (about  $0.3 \text{ g m}^{-2} \text{ yr}^{-1}$ ) is close to the reported value in the western subarctic Pacific ( $0.3 \text{ g m}^{-2} \text{ yr}^{-1}$  [Measures et al., 2005]), and we must be careful about the value. The optimized base scavenging coefficient for  $\text{Fe}_d$  below- and proportionality constant for scavenging of  $\text{Fe}_d$  above- the prescribed ligand concentration of  $0.6 \text{ nmol l}^{-1}$  (see Appendix A, equation (A79)) ( $\lambda_{\text{scav}}$  and  $\gamma_{\text{high}}$ ) are not intuitive for their units. Thus, we calculated well known scavenging rates averaged in ML in addition to the desorption rate ( $\lambda_{\text{desorption}}$ ). The results are shown in Figure 8. The dissolved iron scavenging is formulated as a function of POC and dust fluxes in the model (see Appendix A, equation (A79)), and in the peak diatom bloom period the scavenging rate is maximum and in other seasons the

scavenging rate is low. The residence time of dissolved iron with respect to the scavenging within ML range from about 0.03 to 1 year. The residence time in the bloom season (about 0.03 yr) is consistent with the previous open ocean observations (0.05–0.08 year [Sarhou et al., 2003]; 0.1–0.4 year [Bergquist and Boyle, 2006]). Thus, the present parameters seem to be reasonable.

[32] Desorption rate is much lower than the scavenging rate and is lower than the experimentally estimated value as stated in the previous section. This seems to be needed to maintain the high level of particulate iron in ML and water column inferred from both the data at this study station, and some vertical profiles from January to May 2003 at the nearby station, A7 [Nishioka et al., 2007]. This slow desorption rate might be the compromise for compensating for the 1-D model deficiency which cannot reproduce the probable lateral transport of  $\text{Fe}_p$  as stated above. In the previous modeling research for iron, desorption rate is generally higher than the scavenging rate to reproduce the whole ocean iron distribution [e.g., Parekh et al., 2004]. Thus, the lower desorption rate than the scavenging rate estimated in this study should be checked in the future when embedding the model into the OGCM. Furthermore, recent research has shown that the prescribed ligand concentration was very important for the biogeochemical model to reproduce the high dissolved iron in the intermediate layer of the subarctic Pacific [Misumi et al., 2011]. However, that research did not detail how the change in ligand concentration affected the behavior of iron and biogeochemistry in the upper ocean. It was also reported that the concentration of the ligand could change during phytoplankton blooms in an iron enrichment experiment [Kondo et al., 2008]. There are, however, no observations of the ligand in the present study region, which precludes constraining its modeled concentration. Therefore, we used the value of 0.6 nM as in previous modeling research [Moore et al., 2004; Moore and Braucher, 2008]. No doubt the present value of 0.6 nM will be reconsidered when embedding the model into the OGCM. It will be very important for us to examine the sensitivity of the ligand concentration to  $\text{Fe}_d$  and  $\text{Fe}_p$ , plus  $\text{Fe}_b$  in the mixed layer and we did the sensitivity analysis as stated in the next section. As for the sinking velocity of particulate iron ( $w_{\text{Fcp}}$ ), the velocity needs to be quite slow as stated in section 4.2 to keep the high concentration of particulate iron in ML and water column (Table 1). If we impose the higher value of  $0.1 \text{ m d}^{-1}$  on the

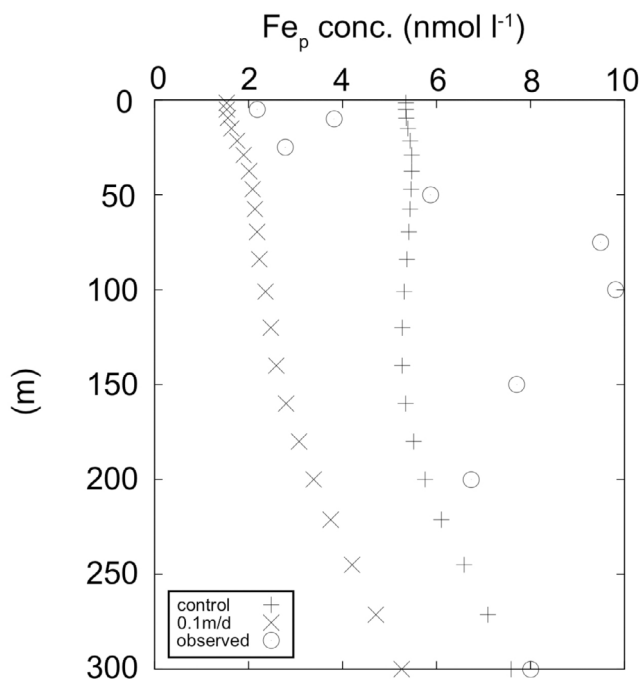


**Figure 9.** Comparisons of annually averaged simulated particulate iron concentration within the upper 300 m between experiments changing the sinking rate. The observed vertical profile was obtained at Station A4 in April 2003 [Nishioka *et al.*, 2007].

sinking velocity, the concentration in and below ML gets too low and the model cannot reproduce the observed high concentration of particulate iron within and below ML (Figure 9). However, the maximum concentration observed at around 100 m could not be reproduced by the model, which might be due to the lateral transport as stated above. The estimated value of  $0.001 \text{ m d}^{-1}$  is close to the value calculated by using the terminal velocity equation for a solid sphere at low Reynolds numbers ( $<1.0$ ) assuming a density for organic matter of  $1.06 \text{ g cm}^{-3}$  (estimated density of a bacterial cell containing 80% water [Logan and Hunt, 1987]), the diameter of  $1 \mu\text{m}$  and seawater density of  $1.024 \text{ g cm}^{-3}$  at  $20^\circ\text{C}$  with salinity of 35. To date, our knowledge about particulate iron measured in the ocean is not enough. In the western subarctic Pacific, the depth of maximum particulate iron concentration has been found to be shallower than the corresponding depth for dissolved iron, and this is thought to be caused by the particulate iron sinking and remineralization [Nishioka *et al.*, 2007] and laterally transported iron in the intermediate layer [Nishioka *et al.*, 2011]. Thus, the estimated slow sinking rate of particulate iron might be a characteristic of this basin and be related to small organic matter particles in terms of the sinking velocity, and/or again compensate for the model deficiency for the present 1-D model not being able to represent the laterally transported particulate iron (Figure 9). Anyway, this must be investigated when incorporating the model into OGCM in the future. Finally, the fraction of remaining scavenged  $\text{Fe}_d$  to  $\text{Fe}_p$  in the model domain ( $f_{\text{Fe}_c}$ ) is unity, i.e., 100% (Table 1; see Appendix A, equation (A80)), which means that all the scavenged  $\text{Fe}_d$  becomes  $\text{Fe}_p$  in the model. This parameter should

also be checked when embedding the model into the OGCM because dust-derived iron continues to accumulate in the model and the iron inventory in the model domain continues to increase with this 100% fraction.

#### 4.4. Sensitivity of Each Parameter Associated With the Iron Cycle to the Modeled Iron in ML

[33] The procedure used to test the sensitivity of each parameter value to  $\text{Fe}_d$ , and  $\text{Fe}_p$  plus  $\text{Fe}_b$  concentrations annually averaged in ML is the same as in Fasham *et al.* [1990]. In this sensitivity analysis, we considered the ligand concentration ( $C_{\text{ligand}}$ ) which was prescribed to be  $0.6 \text{ nM}$  in the model in addition to the optimized parameters. In brief, we examine the sensitivity of each parameter in turn by running the model with the parameter altered to half and twice the optimized or prescribed value. In this way, it was possible to determine which parameters had the large effects on which prognostic variables for iron. The sensitivity was quantified by calculating the following normalized sensitivity defined as the percentage change in a state variable produced by a percentage change in the parameter. The sensitivity of a given parameter,  $p$ , was quantified by calculating the normalized sensitivity,  $S(p)$ , defined as,

$$S(p) = \left( \frac{E(p) - E_s}{E_s} \right) / \left( \frac{p - p_s}{p_s} \right), \quad (4)$$

where  $E_s$  is the annually averaged  $\text{Fe}_d$  or  $\text{Fe}_p$  plus  $\text{Fe}_b$  concentration in ML for the control case with the optimized or prescribed parameter value  $p_s$ , and  $E(p)$  is the correspondence for the case when the parameter is set at the value  $p$ . This index measures the fractional change in the statistic for a fractional change in the parameter. Sensitivities for  $\text{Fe}_d$ , and  $\text{Fe}_p$  plus  $\text{Fe}_b$  annually averaged in ML are shown in Table 2.

[34] For  $\text{Fe}_d$ , the most sensitive parameter is the potential maximum growth rate of PL ( $V_{0,\text{PL}}$ ) and the second most sensitive parameter is the remineralization and decomposition rates of PON ( $V_{\text{PDOS}}$ ,  $V_{\text{PAOS}}$ ,  $V_{\text{PDOL}}$ ,  $V_{\text{PAOL}}$ ). As seen in Figure 4, in the present model, PL is the predominant phytoplankton and that the parameter is the most sensitive makes sense. In addition, the remineralization and decomposition of PON produced by PL also affect  $\text{Fe}_d$  to a large extent. The potential maximum growth rate of PS ( $V_{0,\text{PS}}$ ), minimum sinking velocity of PON and Opal ( $w_{\text{min}}^{\text{PON}_L}$ ,  $w_{\text{min}}^{\text{Opal}}$ ), the stoichiometric ratio of iron to nitrogen ( $R_{\text{FeN}}$ ) and dust-derived iron solubility ( $\alpha$ ) have relatively large impacts on  $\text{Fe}_d$  in ML. As seen in Figure 4, from late spring to summer the NPP and biomass of PS increase in opposition to the decreases of those of PL. Thus,  $V_{0,\text{PS}}$  also has a relatively large impact on  $\text{Fe}_d$  in ML. In this study, we think that the parameters associated with OU kinetics for both PS and PL are not well constrained because there are no available size-fractionated data, such as biomass, Chl. *a* or NPP. Thus, these parameters need to be constrained in the future.  $w_{\text{min}}^{\text{PON}_L}$  and  $w_{\text{min}}^{\text{Opal}}$  are found to be the sensitive parameters, and that is intuitive because these sinking velocities affect the degree to which  $\text{PON}_L$  and Opal remineralizes/decomposes and dissolves in ML, respectively, which affects  $\text{Fe}_d$  in ML.  $R_{\text{FeN}}$  is also a critical parameter for determining  $\text{Fe}_d$  in the model. This is also intuitive because this parameter determines the way of utilizing nitrogenous nutrients and  $\text{Fe}_d$  by phytoplankton.  $\alpha$  is directly related to the dust-derived iron

**Table 2.** Normalized Parameter Sensitivity of Annually Averaged  $\text{Fe}_d$  and  $\text{Fe}_p$  Plus  $\text{Fe}_b$  Within the Mixed Layer for Each Parameter<sup>a</sup>

Parameter	Parameter Range Used for Optimization	Standard Value	Normalized Sensitivity	
			$\text{Fe}_d$ in the ML	$\text{Fe}_p+\text{Fe}_b$ in the ML
$V_{0,PS}$	0.1/3.2	0.6	0.01, -0.15	0.00, 0.01
$A_{0,NO_3,PS}$	1/512	282	-0.01, -0.03	0.00, 0.00
$V_{0,PL}$	0.1/3.2	0.8	-0.64, -0.24	0.02, 0.01
$A_{0,NO_3,PL}$	1/512	252	-0.06, -0.05	0.00, 0.00
$w_{PON_s}^{min}, w_{PON_s}^{max}$	3/48	6	-0.24, -0.10	0.01, 0.00
$w_{PON_L}^{min}, w_{PON_L}^{max}$	48/198	198	-0.05, -0.02	0.00, 0.00
$V_{PDOS}, V_{PAOS}, V_{PDOL}, V_{PAOL}$	0.01/0.32	0.08	0.19, 0.30	0.00, -0.01
$V_{DAO}$	0.01/0.32	0.15	-0.01, 0.00	0.00, 0.00
$V_{Opal}$	0.01/0.32	0.16	-0.04, 0.00	0.00, 0.00
$R_{FeN}$	$1.0 \times 10^{-5}/7.3 \times 10^{-5}$	$1.7 \times 10^{-5}$	-0.12, -0.14	-0.02, -0.01
$R_{SiNL}$	1.0/4.1	3.6	0.00, -0.01	0.00, 0.00
$R_{SiNH}$	1.0/1.7	1.0	0.00, 0.03	0.00, 0.00
$Fe_{SiN}^*$	0.01/0.63	0.03	0.00, 0.00	0.00, 0.00
$\alpha$	1.0/4.5	4.0	0.10, 0.10	0.02, 0.02
$\lambda_{desorption}$	0.001/0.128	0.003	0.00, 0.00	0.00, 0.00
$\lambda_{scav}$	0.001/0.256	0.185	0.01, -0.01	0.00, 0.00
$\gamma_{high}$	0.0001/0.0256	0.0044	0.00, 0.00	0.00, 0.00
$w_{Fep}$	0.001/0.128	0.001	0.00, 0.00	0.00, 0.00
$f_{Fep}$	0.3/1.0	1.0	-0.02	-0.03
$C_{ligand}$		0.6	-0.04, 0.02	0.00, 0.00

<sup>a</sup>This index measures the fractional change in the statistic for a fractional change in the parameter (see text).

dissolution mostly at the surface of the model domain. Thus, this parameter is also critical for the  $\text{Fe}_d$ . Other optimized parameters including the ligand concentration ( $C_{ligand}$ ) had no remarkable impacts on  $\text{Fe}_d$ .

[35] As for  $\text{Fe}_p$  plus  $\text{Fe}_b$ , all the optimized parameters in addition to the ligand concentration have smaller effects on the concentration in ML compared to  $\text{Fe}_d$ . However,  $w_{Fep}$  is an important parameter for  $\text{Fe}_p$  concentration in the upper ocean as stated in section 4.3. Thus, we will have to check this parameter when embedding the model into the OGCM.

## 5. Conclusion

[36] We have developed a 1-D ecosystem model consisting of 14 compartments including the iron cycle and applied it to Station A4 in the Oyashio region of the western subarctic Pacific, in order to understand the iron cycle there and investigate the model performance. Data-assimilative approach was used to constrain the parameters associated with the iron cycle. The model was able to successfully reproduce the observations and demonstrated especially the following characteristics of the seasonal variations and relationships of  $\text{Fe}_d$ , silicate and nitrate in the ML: (1) The high  $\text{Fe}_d$  concentration in the ML in winter is mainly due to the vertical winter mixing (entrainment), which supplies more  $\text{Fe}_d$  to the ML than any other sources on an annual cycle, (2) uptake by diatoms during the spring bloom rapidly reduces  $\text{Fe}_d$  concentration in the ML to near-depletion, which results in an increasing consumption ratio of silicate to nitrogenous nutrients by diatoms, causing more rapid decrease of silicate compared to nitrogenous nutrients in the ML. This shift in the consumption ratio leads to iron limitation of diatoms during the peak spring bloom, followed by silicate limitation. (3)  $\text{Fe}_d$  in the ML supplied by dust dissolution and desorption from particulate iron somewhat alleviates iron limitation of phytoplankton, thereby supporting the continuous utilization of nitrate in the ML from spring to fall, even though  $\text{Fe}_d$  concentration in the ML remains low.

The model also reproduces well the observed high total particulate iron concentration in the upper ocean, but the observed vertical profile of particulate iron with a maximum around 100 m depth cannot be reproduced by the present 1-D model. This apparent model deficiency seems to result in extremely slow sinking velocity and desorption rate of  $\text{Fe}_p$  in the data-based optimization. We will further investigate this apparent deficiency of the present 1-D model in the near future when embedding it into the OGCM.

## Appendix A

### A1. Nitrogen, Silicon and Iron Regulated Marine Ecosystem Model (NSI-MEM)

[37] This ecosystem model is mainly based on the NEMURO model which was previously developed and applied to the North Pacific [Yamanaka *et al.*, 2004; Kishi *et al.*, 2007]. In this study, we modified and extended the model in order to investigate the dynamics of bioelements, such as nitrogen, silicon and iron in the ocean.

[38] The unit used for each prognostic variable is as follows: for non-diatom small phytoplankton (PS), diatoms (PL), micro-zooplankton (ZS), meso-zooplankton (ZL), predatory zooplankton (ZP), nitrate ( $\text{NO}_3$ ), ammonium ( $\text{NH}_4$ ), small/large particulate organic nitrogen ( $\text{PON}_s$ ,  $\text{PON}_L$ ), dissolved organic nitrogen (DON) in  $\text{molN l}^{-1}$ ; for silicate ( $\text{Si(OH)}_4$ ) and biogenic silica (Opal) in  $\text{molSi l}^{-1}$ ; for dissolved iron ( $\text{Fe}_d$ ) and particulate iron ( $\text{Fe}_p$ ) in  $\text{molFe l}^{-1}$ . The prognostic variables are calculated as a function of time,  $t$ , and depth,  $z$ . The governing equations for nitrogen, silicon and iron fluxes except for physical terms are listed below.

$$\begin{aligned} \frac{d[\text{PS}]}{dt} = & (\text{PS photosynthesis}) - (\text{PS respiration}) \\ & - (\text{PS extracellular excretion}) - (\text{PS mortality}) \\ & - (\text{PS grazing by ZS}) - (\text{PS grazing by ZL}), \end{aligned} \quad (\text{A1})$$

$$\begin{aligned} \frac{d[\text{PL}]}{dt} = & (\text{PL photosynthesis}) - (\text{PL respiration}) \\ & - (\text{PL extracellular excretion}) - (\text{PL mortality}) \\ & - (\text{PL grazing by ZL}) - (\text{PL grazing by ZP}), \end{aligned} \quad (\text{A2})$$

$$\begin{aligned} \frac{d[\text{ZS}]}{dt} = & (\text{PS grazing by ZS}) - (\text{ZS excretion}) - (\text{ZS egestion}) \\ & - (\text{ZS mortality}) - (\text{ZS predation by ZL}) \\ & - (\text{ZS predation by ZP}), \end{aligned} \quad (\text{A3})$$

$$\begin{aligned} \frac{d[\text{ZL}]}{dt} = & (\text{PS grazing by ZL}) + (\text{PL grazing by ZL}) \\ & + (\text{ZS predation by ZL}) - (\text{ZL excretion}) \\ & - (\text{ZL egestion}) - (\text{ZL mortality}) \\ & - (\text{ZL predation by ZP}), \end{aligned} \quad (\text{A4})$$

$$\begin{aligned} \frac{d[\text{ZP}]}{dt} = & (\text{PL grazing by ZP}) + (\text{ZS predation by ZP}) \\ & + (\text{ZL predation by ZP}) - (\text{ZP excretion}) \\ & - (\text{ZP egestion}) - (\text{ZP mortality}), \end{aligned} \quad (\text{A5})$$

$$\begin{aligned} \frac{d[\text{NO}_3]}{dt} = & (\text{nitrification}) - \{(\text{PS photosynthesis}) \\ & - (\text{PS respiration})\} \times R_{\text{newS}} - \{(\text{PL photosynthesis}) \\ & - (\text{PL respiration})\} \times R_{\text{newL}}, \end{aligned} \quad (\text{A6})$$

$$\begin{aligned} \frac{d[\text{NH}_4]}{dt} = & (\text{ZS excretion}) + (\text{ZL excretion}) + (\text{ZP excretion}) \\ & + (\text{DON remineralization}) + (\text{PON}_S \text{ remineralization}) \\ & + (\text{PON}_L \text{ remineralization}) - (\text{nitrification}) \\ & - \{(\text{PS photosynthesis}) - (\text{PS respiration})\} \\ & \times (1 - R_{\text{newS}}) - \{(\text{PL photosynthesis}) \\ & - (\text{PL respiration})\} \times (1 - R_{\text{newL}}), \end{aligned} \quad (\text{A7})$$

$$\begin{aligned} \frac{d[\text{PON}_S]}{dt} = & (\text{PS mortality}) + 0.5(\text{PL mortality}) + (\text{ZS mortality}) \\ & + (\text{ZS egestion}) - (\text{PON}_S \text{ remineralization}) \\ & - (\text{PON}_S \text{ decomposition to DON}) \\ & + (\text{PON}_S \text{ settlement}) \\ & + (\text{Aggregation of DON to PON}_S) \\ & - (\text{Aggregation of PON}_S \text{ to PON}_L), \end{aligned} \quad (\text{A8})$$

$$\begin{aligned} \frac{d[\text{PON}_L]}{dt} = & 0.5(\text{PL mortality}) + (\text{ZL mortality}) + (\text{ZP mortality}) \\ & + (\text{ZL egestion}) + (\text{ZP egestion}) \\ & - (\text{PON}_L \text{ remineralization}) \\ & - (\text{PON}_L \text{ decomposition to DON}) \\ & + (\text{PON}_L \text{ settlement}) \\ & + (\text{Aggregation of DON to PON}_L) \\ & + (\text{Aggregation of PON}_S \text{ to PON}_L), \end{aligned} \quad (\text{A9})$$

$$\begin{aligned} \frac{d[\text{DON}]}{dt} = & (\text{PS extracellular excretion}) \\ & + (\text{PL extracellular excretion}) \\ & + (\text{PON}_S \text{ decomposition to DON}) \\ & + (\text{PON}_L \text{ decomposition to DON}) \\ & - (\text{Aggregation of DON to PON}_S) \\ & - (\text{Aggregation of DON to PON}_L) \\ & - (\text{DON remineralization}), \end{aligned} \quad (\text{A10})$$

$$\frac{d[\text{Si}(\text{OH})_4]}{dt} = (\text{Opal dissolution}) - (\text{Opal formation}), \quad (\text{A11})$$

$$\begin{aligned} \frac{d[\text{Opal}]}{dt} = & (\text{Opal egestion by ZL}) + (\text{Opal egestion by ZP}) \\ & + (\text{Opal derived from PL mortality}) \\ & - (\text{Opal dissolution}) + (\text{Opal settlement}), \end{aligned} \quad (\text{A12})$$

$$\begin{aligned} \frac{d[\text{Fe}_d]}{dt} = & \left[ \frac{d[\text{NO}_3]}{dt} + \frac{d[\text{NH}_4]}{dt} \right] \times R_{\text{FeN}} + (\text{Dust dissolution}) \\ & + (\text{Fe}_p \text{ desorption}) - (\text{Fe}_d \text{ scavenging}), \end{aligned} \quad (\text{A13})$$

$$\begin{aligned} \frac{d[\text{Fe}_p]}{dt} = & (\text{Fe}_d \text{ scavenging}) - (\text{Fe}_p \text{ desorption}) + (\text{Fe}_p \text{ settlement}) \\ & - (\text{Fe}_p \text{ burial}). \end{aligned} \quad (\text{A14})$$

## A2. Formulation of Each Source/Sink Process

[39] In the following, the model's source minus sink (sms) equations are listed, and parameter values described below are shown in Table A1.

[40] Photosynthesis of PS is determined by temperature ( $T$ , °C),  $\text{NH}_4$ ,  $\text{NO}_3$ ,  $\text{Fe}_d$  and photosynthetically active radiation ( $I$ ,  $\text{W m}^{-2}$ ) to which solar radiation in the model is converted by multiplying by 0.45 as in *Fujii et al.* [2007], and is expressed as

$$(\text{PS photosynthesis}) = \min\left(\mu_{\text{N}}^{\text{PS}}, \mu_{\text{Fe}_d}^{\text{PS}}\right) L_{f,\text{PS}}(I) \exp(k_{\text{PS}} T) [\text{PS}], \quad (\text{A15})$$

where  $\mu_{\text{N}}^{\text{PS}}$  and  $\mu_{\text{Fe}_d}^{\text{PS}}$  are nitrogen ( $\text{NH}_4$  and  $\text{NO}_3$ ) and dissolved iron limited growth rates, respectively, and  $L_{f,\text{PS}}(I)$  is a non-dimensional light limiting factor.  $\mu_{\text{N}}^{\text{PS}}$  and  $\mu_{\text{Fe}_d}^{\text{PS}}$  are calculated based on the Optimum Uptake (OU) kinetics for nutrients proposed by *Smith and Yamanaka* [2007] and *Smith et al.* [2009] as follows:

$$\mu_{\text{N}}^{\text{PS}} = \frac{V_{0,\text{PS}}[\text{NO}_3]}{\frac{[\text{NO}_3]}{1-f_{\text{AS}}} + \frac{V_{0,\text{PS}}}{f_{\text{AS}}A_{0,\text{NO}_3,\text{PS}}}} \left(1 - \frac{[\text{NH}_4]}{[\text{NH}_4] + K_{\text{NH}_4,\text{PS}}}\right) + \frac{V_{0,\text{PS}}[\text{NH}_4]}{\frac{[\text{NH}_4]}{1-f_{\text{AS}}} + \frac{V_{0,\text{PS}}}{f_{\text{AS}}A_{0,\text{NH}_4,\text{PS}}}}, \quad (\text{A16})$$

$$\mu_{\text{Fe}_d}^{\text{PS}} = \frac{V_{0,\text{PS}}[\text{Fe}_d]}{\frac{[\text{Fe}_d]}{1-f_{\text{AS}}} + \frac{V_{0,\text{PS}}}{f_{\text{AS}}A_{0,\text{Fe}_d,\text{PS}}}}, \quad (\text{A17})$$

where  $V_{0,\text{PS}}$ ,  $A_{0,\text{NO}_3,\text{PS}}$ ,  $A_{0,\text{NH}_4,\text{PS}}$  and  $A_{0,\text{Fe}_d,\text{PS}}$  are the potential maximum growth rate of PS, and potential maximum affinity

**Table A1.** Model Parameters

Parameter	Symbol	Value	Unit <sup>a</sup>	Source <sup>b</sup>
<i>Underwater Light Dissipation</i>				
Light dissipation coefficient of seawater	$\alpha_1$	0.04	$\text{m}^{-1}$	1
Self shading coefficient by phytoplankton	$\alpha_2$	0.04	$1 \mu\text{molN}^{-1} \text{m}^{-1}$	1
<i>Non-diatom Small Phytoplankton (PS)</i>				
Initial slope of photosynthesis-irradiance curve	$\alpha_{\text{PS}}$	0.013	$\text{W}^{-1} \text{m}^2 \text{day}^{-1}$	5
Photoinhibition index	$\beta_{\text{PS}}$	$1.4 \times 10^{-15}$	$\text{W}^{-1} \text{m}^2 \text{day}^{-1}$	5
Potential maximum light-saturated photosynthetic rate	$P_{\text{S,PS}}$	0.4	$\text{day}^{-1}$	5
Potential maximum growth rate at 0°C	$V_{0,\text{PS}}$	Opt.	$\text{day}^{-1}$	5
Potential maximum affinity for $\text{NO}_3$	$A_{0,\text{NO}_3,\text{PS}}$	Opt.	$1 \text{molN}^{-1} \text{s}^{-1}$	5
Temperature coefficient for photosynthetic rate	$k_{\text{PS}}$	0.0693	$^{\circ}\text{C}^{-1}$	1
Mortality rate at 0°C	$M_{\text{PS0}}$	0.0585	$1 \mu\text{molN}^{-1} \text{day}^{-1}$	1
Temperature coefficient for mortality	$k_{\text{MS}}$	0.0693	$^{\circ}\text{C}^{-1}$	1
Respiration rate at 0°C	$R_{\text{PS0}}$	0.03	$\text{day}^{-1}$	1
Temperature coefficient for respiration	$k_{\text{RS}}$	0.0519	$^{\circ}\text{C}^{-1}$	1
Ratio of extracellular excretion to photosynthesis	$\gamma_{\text{S}}$	0.135	(Nodim)	1
<i>Diatoms (PL)</i>				
Initial slope of photosynthesis-irradiance curve	$\alpha_{\text{PL}}$	0.045	$\text{W}^{-1} \text{m}^2 \text{day}^{-1}$	5
Photoinhibition index	$\beta_{\text{PL}}$	$1.4 \times 10^{-15}$	$\text{W}^{-1} \text{m}^2 \text{day}^{-1}$	5
Potential maximum light-saturated photosynthetic rate	$P_{\text{S,PL}}$	1.4	$\text{day}^{-1}$	5
Potential maximum growth rate at 0°C	$V_{0,\text{PL}}$	Opt.	$\text{day}^{-1}$	5
Potential maximum affinity for $\text{NO}_3$	$A_{0,\text{NO}_3,\text{PL}}$	Opt.	$1 \text{molN}^{-1} \text{s}^{-1}$	5
Temperature coefficient for photosynthetic rate	$k_{\text{PL}}$	0.0693	$^{\circ}\text{C}^{-1}$	1
Mortality rate at 0°C	$M_{\text{PL0}}$	0.029	$1 \mu\text{molN}^{-1} \text{day}^{-1}$	1
Temperature coefficient for mortality	$k_{\text{ML}}$	0.0693	$^{\circ}\text{C}^{-1}$	1
Respiration rate at 0°C	$R_{\text{PL0}}$	0.03	$\text{day}^{-1}$	1
Temperature coefficient for respiration	$k_{\text{RL}}$	0.0519	$^{\circ}\text{C}^{-1}$	1
Ratio of extracellular excretion to photosynthesis	$\gamma_{\text{L}}$	0.135	(Nodim)	1
<i>Microzooplankton (ZS)</i>				
Maximum rate of grazing PS at 0°C	$G_{\text{RmaxS}}$	0.4	$\text{day}^{-1}$	1
Temperature coefficient for grazing	$k_{\text{GS}}$	0.693	$^{\circ}\text{C}^{-1}$	1
Ivlev constant	$\lambda_{\text{S}}$	1.4	$1 \mu\text{molN}^{-1}$	1
Threshold value for grazing PS	$\text{PS}_{\text{ZS}}^*$	0.043	$\mu\text{molN l}^{-1}$	1
Assimilation efficiency	$\alpha_{\text{ZS}}$	0.7	(Nodim)	1
Growth efficiency	$\beta_{\text{ZS}}$	0.3	(Nodim)	1
Mortality rate at 0°C	$M_{\text{ZS0}}$	0.0585	$1 \mu\text{molN}^{-1} \text{day}^{-1}$	1
Temperature coefficient for mortality	$k_{\text{MZS}}$	0.0693	$^{\circ}\text{C}^{-1}$	1
<i>Mesozooplankton (ZL)</i>				
Maximum rate of grazing PS at 0°C	$G_{\text{RmaxL,PS}}$	0.1	$\text{day}^{-1}$	1
Maximum rate of grazing PL at 0°C	$G_{\text{RmaxL,PL}}$	0.4	$\text{day}^{-1}$	1
Maximum predation rate of ZS at 0°C	$G_{\text{RmaxL,ZS}}$	0.4	$\text{day}^{-1}$	1
Temperature coefficient for grazing/predation	$k_{\text{GL}}$	0.0693	$^{\circ}\text{C}^{-1}$	1
Ivlev constant	$\lambda_{\text{L}}$	1.4	$1 \mu\text{molN}^{-1}$	1
Threshold value for grazing PS	$\text{PS}_{\text{ZL}}^*$	0.043	$\mu\text{molN l}^{-1}$	1
Threshold value for grazing PL	$\text{PL}_{\text{ZL}}^*$	0.043	$\mu\text{molN l}^{-1}$	1
Threshold value for predation of ZS	$\text{ZS}_{\text{ZL}}^*$	0.043	$\mu\text{molN l}^{-1}$	1
Assimilation efficiency	$\alpha_{\text{ZL}}$	0.7	(Nodim)	1
Growth efficiency	$\beta_{\text{ZL}}$	0.3	(Nodim)	1
Mortality rate at 0°C	$M_{\text{ZL0}}$	0.0585	$1 \mu\text{molN}^{-1} \text{day}^{-1}$	1
Temperature coefficient for mortality	$k_{\text{MZL}}$	0.0693	$^{\circ}\text{C}^{-1}$	1
<i>Predatory Zooplankton (ZP)</i>				
Maximum rate of grazing PL at 0°C	$G_{\text{RmaxP,PL}}$	0.2	$\text{day}^{-1}$	1
Maximum predation rate of ZS at 0°C	$G_{\text{RmaxP,ZS}}$	0.2	$\text{day}^{-1}$	1
Maximum predation rate of ZL at 0°C	$G_{\text{RmaxP,ZL}}$	0.4	$\text{day}^{-1}$	2
Temperature coefficient for grazing/predation	$k_{\text{GP}}$	0.0693	$^{\circ}\text{C}^{-1}$	1
Ivlev constant	$\lambda_{\text{P}}$	1.4	$1 \mu\text{molN}^{-1}$	1
Threshold value for grazing PL	$\text{PL}_{\text{ZP}}^*$	0.043	$\mu\text{molN l}^{-1}$	1
Threshold value for predation of ZS	$\text{ZS}_{\text{ZP}}^*$	0.043	$\mu\text{molN l}^{-1}$	1
Threshold value for predation of ZL	$\text{ZL}_{\text{ZP}}^*$	0.043	$\mu\text{molN l}^{-1}$	1
Preference coefficient for PL	$\Psi_{\text{PL}}$	4.605	$1 \mu\text{molN}^{-1}$	1
Preference coefficient for ZS	$\Psi_{\text{ZS}}$	3.01	$1 \mu\text{molN}^{-1}$	1
Assimilation efficiency	$\alpha_{\text{ZP}}$	0.7	(Nodim)	1
Growth efficiency	$\beta_{\text{ZP}}$	0.3	(Nodim)	1
Mortality rate at 0°C	$M_{\text{ZP0}}$	0.0585	$1 \mu\text{molN}^{-1} \text{day}^{-1}$	1
Temperature coefficient for mortality	$k_{\text{MZP}}$	0.0693	$^{\circ}\text{C}^{-1}$	1

**Table A1.** (continued)

Parameter	Symbol	Value	Unit <sup>a</sup>	Source <sup>b</sup>
<i>Nitrification</i>				
Nitrification rate at 0°C	$V_{\text{Nit0}}$	0.03	day <sup>-1</sup>	1
Temperature coefficient for nitrification	$k_{\text{Nit}}$	0.0693	°C <sup>-1</sup>	1
<i>Remineralization and Decomposition</i>				
PON <sub>S</sub> sinking velocity	$w_{\text{PON}_S}^{\text{PON}_S}$	3.0	m day <sup>-1</sup>	3
PON <sub>L</sub> minimum sinking velocity	$w_{\text{PON}_L}^{\text{PON}_L}$	Opt.	m day <sup>-1</sup>	5
PON <sub>L</sub> maximum sinking velocity	$w_{\text{PON}_L}^{\text{min}}$	Opt.	m day <sup>-1</sup>	5
Decomposition rate of PON <sub>S</sub> to DON at 0°C	$V_{\text{PDOS}}$	Opt.	day <sup>-1</sup>	5
Temperature coefficient for PON <sub>S</sub> decomposition to DON	$k_{\text{PDS}}$	0.0693	°C <sup>-1</sup>	1
Remineralization rate of PON <sub>S</sub> at 0°C	$V_{\text{PAOS}}$	Opt.	day <sup>-1</sup>	5
Temperature coefficient for PON <sub>S</sub> remineralization	$k_{\text{PAS}}$	0.0693	°C <sup>-1</sup>	1
Decomposition rate of PON <sub>L</sub> to DON at 0°C	$V_{\text{PDOL}}$	Opt.	day <sup>-1</sup>	5
Temperature coefficient for PON <sub>L</sub> decomposition to DON	$k_{\text{PDL}}$	0.0693	°C <sup>-1</sup>	1
Remineralization rate of PON <sub>L</sub> at 0°C	$V_{\text{PAL}}$	Opt.	day <sup>-1</sup>	5
Temperature coefficient for PON <sub>L</sub> remineralization	$k_{\text{PAL}}$	0.0693	°C <sup>-1</sup>	1
Remineralization rate of DON at 0°C	$V_{\text{DA0}}$	Opt.	day <sup>-1</sup>	5
Temperature coefficient for DON decomposition to NH <sub>4</sub>	$k_{\text{DA}}$	0.0693	°C <sup>-1</sup>	1
<i>Opal</i>				
Opal minimum sinking velocity	$w_{\text{Opal}}^{\text{Opal}}$	Opt.	m day <sup>-1</sup>	5
Opal maximum sinking velocity	$w_{\text{Opal}}^{\text{min}}$	Opt.	m day <sup>-1</sup>	5
Dissolution rate of Opal at 0°C	$V_{\text{Opal}}$	Opt.	day <sup>-1</sup>	5
Temperature coefficient for Opal decomposition	$k_{\text{Opal}}$	0.0693	°C <sup>-1</sup>	1
<i>Stoichiometric Ratio</i>				
Stoichiometry of carbon to nitrogen	$R_{\text{CN}}$	6.625	molC/molN	1
Stoichiometry of iron to nitrogen	$R_{\text{FeN}}$	Opt.	molFe/molN	5
PL stoichiometry of silicate to nitrogenous nutrients uptake in iron-replete condition	$R_{\text{SiNH}}$	Opt.	molSi/molN	5
PL stoichiometry of silicate to nitrogenous nutrients uptake in iron-deficient condition	$R_{\text{SiNL}}$	Opt.	molSi/molN	5
Threshold dissolved iron value for shift in RSiNH to RSiNL	$\text{Fe}_{\text{SiN}}^*$	Opt.	nmol l <sup>-1</sup>	5
<i>Aggregation</i>				
Aggregation rate for DON to PON <sub>S</sub> by shear	$\phi_1^{\text{DON}}, \phi_2^{\text{DON}}$	530, 4624	1 μmolN <sup>-1</sup>	3
Aggregation rate for DON to PON <sub>L</sub> by shear	$\phi_3^{\text{DON}}$	69562	1 μmolN <sup>-1</sup>	3
Aggregation rate for PON <sub>S</sub> to PON <sub>L</sub> by shear	$\phi_1^{\text{PON}_S}, \phi_2^{\text{PON}_S}$	6228, 69828	1 μmolN <sup>-1</sup>	3
Aggregation rate for PON <sub>S</sub> to PON <sub>L</sub> by differential settlement	$\phi_3^{\text{PON}_S}, \phi_4^{\text{PON}_S}$	0, 4.37	1 μmolN <sup>-1</sup> day <sup>-1</sup>	3
<i>Iron</i>				
Iron atomic weight	$A_{w,\text{Fe}}$	55.847	g mol <sup>-1</sup>	-
Iron content in dust	$C_{\text{iron}}$	3.5	%	6
Solubility of iron in dust at the sea surface layer	$\alpha$	Opt.	%	5
Fraction of Fe <sub>p</sub> not removed to sediment	$f_{\text{Fe}_p}$	Opt.	(Nodim)	5
Fraction of hard dust	$f_{\text{hard}}$	0.97	(Nodim)	4
Dissolution length scale for soft dust	$\delta_{\text{soft\_dust}}$	600	m	4
Dissolution length scale for hard dust	$\delta_{\text{hard\_dust}}$	40000	m	4
Desorption rate at 30°C	$\lambda_{\text{desorption}}$	Opt.	day <sup>-1</sup>	5
Slope of Arrhenius relation	$A_E$	4000	K	4
Reference temperature for Arrhenius relation	$T_{\text{ref}}$	303.15	K	5
Base scavenging coefficient	$\lambda_{\text{scav}}$	Opt.	cm <sup>2</sup> ng <sup>-1</sup>	5
Total ligand concentration	$C_{\text{ligand}}$	0.6	nmol l <sup>-1</sup>	4
Proportionality constant for scavenging of Fe <sub>d</sub>	$\gamma_{\text{high}}$	Opt.	l nmol <sup>-1</sup> day <sup>-1</sup>	5
Particulate iron sinking velocity	$w_{\text{Fep}}$	Opt.	m day <sup>-1</sup>	5

<sup>a</sup>“Nodim” means non-dimensional.

<sup>b</sup>Sources noted here are as follows: 1, *Yamanaka et al.* [2004]; 2, *Fujii et al.* [2007]; 3, *Aumont and Bopp* [2006]; 4, *Moore and Braucher* [2008]; 5, this study (“Opt.” means that the parameter was optimized in this study); 6, *Zhu et al.* [1997].

of PS for NO<sub>3</sub>, NH<sub>4</sub> and Fe<sub>d</sub>, respectively, and  $f_{\text{AS}}$  represents the fraction of internal resources (nitrogen) allocated to the cellular surface sites of PS. For inhibition of nitrate uptake by ammonium, the parameterization of *Vallina and Le Quééré* [2008] is used. In this study,  $A_{0,\text{NO}_3,\text{PS}}$  is optimized, and  $A_{0,\text{NH}_4,\text{PS}}$ , and  $f_{\text{AS}}$  are expressed as follows:

$$A_{0,\text{NH}_4,\text{PS}} = A_{0,\text{NO}_3,\text{PS}} \frac{K_{\text{NO}_3,\text{PS}}}{K_{\text{NH}_4,\text{PS}}}, \quad (\text{A18})$$

$$A_{0,\text{Fe}_d,\text{PS}} = A_{0,\text{NO}_3,\text{PS}} \frac{K_{\text{NO}_3,\text{PS}}}{K_{\text{Fe}_d,\text{PS}}}, \quad (\text{A19})$$

where  $K_{\text{NO}_3,\text{PS}}$  (1.0 μmol l<sup>-1</sup>),  $K_{\text{NH}_4,\text{PS}}$  (0.1 μmol l<sup>-1</sup>),  $K_{\text{Fe}_d,\text{PS}}$  (0.05 nmol l<sup>-1</sup>) are values of Michaelis-Menten half-saturation constants as estimated in previous studies [*Yamanaka et al.*, 2004; *Takeda et al.*, 2006]. Thus, the ratios of affinities for different nutrients, which determine which

nutrient will be limiting upon nutrient depletion, are kept consistent with the parameterizations of previous studies. Although with affinity-based kinetics, values of the potential maximum affinity,  $A_{0,\text{NH}_4,\text{PS}}$  and  $A_{0,\text{Fe}_d,\text{PS}}$  can be obtained from experimental data, just as half-saturation constants can be obtained by fits to the Michaelis-Menten equation, few estimates of affinity-based parameters exist for large-scale modeling. We therefore calculate initial estimates for potential maximum affinities based on existing estimates of Michaelis-Menten (MM) half saturation constants from previous modeling research.

$$f_{\text{AS}} = \max \left[ \left( 1 + \sqrt{\frac{\max(A_{0,\text{NO}_3,\text{PS}}[\text{NO}_3], A_{0,\text{NH}_4,\text{PS}}[\text{NH}_4])}{V_{0,\text{PS}}}} \right)^{-1}, \right. \\ \left. \left( 1 + \sqrt{\frac{A_{0,\text{Fe}_d,\text{PS}}[\text{Fe}_d]}{V_{0,\text{PS}}}} \right)^{-1} \right]. \quad (\text{A20})$$

Equation (A20) for  $f_{\text{AS}}$  stipulates that acclimation occurs with respect to the limiting nutrient only.

[41] For the non-dimensional light limiting factor of PS, the formula of *Platt et al.* [1980] is used,

$$L_{f,\text{PS}}(I) = \frac{\left\{ 1 - \exp\left(-\frac{\alpha_{\text{PS}} I}{P_{\text{S,PS}}}\right) \right\} \exp\left(-\frac{\beta_{\text{PS}} I}{P_{\text{S,PS}}}\right)}{\left(\frac{\alpha_{\text{PS}}}{\alpha_{\text{PS}} + \beta_{\text{PS}}}\right) \left(\frac{\beta_{\text{PS}}}{\alpha_{\text{PS}} + \beta_{\text{PS}}}\right)^{\beta_{\text{PS}}/\alpha_{\text{PS}}}}, \quad (\text{A21})$$

in which  $\alpha_{\text{PS}}$ ,  $\beta_{\text{PS}}$  and  $P_{\text{S,PS}}$  denote initial slope of the photosynthesis-irradiance ( $P$ - $E$ ) curve, photoinhibition index, and potential maximum light-saturated photosynthetic rate under the prevailing condition. F-ratio of PS ( $R_{\text{newS}}$ ) can be defined as

$$R_{\text{newS}} = \frac{\frac{V_{0,\text{PS}}[\text{NO}_3]}{\frac{[\text{NO}_3]}{1-f_{\text{AS}}} + \frac{V_{0,\text{PS}}}{f_{\text{AS}}A_{0,\text{NO}_3,\text{PS}}}} \left( 1 - \frac{[\text{NH}_4]}{[\text{NH}_4] + K_{\text{NH}_4,\text{PS}}} \right)}{\frac{V_{0,\text{PS}}[\text{NO}_3]}{\frac{[\text{NO}_3]}{1-f_{\text{AS}}} + \frac{V_{0,\text{PS}}}{f_{\text{AS}}A_{0,\text{NO}_3,\text{PS}}}} \left( 1 - \frac{[\text{NH}_4]}{[\text{NH}_4] + K_{\text{NH}_4,\text{PS}}} \right) + \frac{V_{0,\text{PS}}[\text{NH}_4]}{\frac{[\text{NH}_4]}{1-f_{\text{AS}}} + \frac{V_{0,\text{PS}}}{f_{\text{AS}}A_{0,\text{NH}_4,\text{PS}}}}}. \quad (\text{A22})$$

Photosynthesis of PL is determined as in that of PS except that PL photosynthesis is also dependent on silicate.

$$(\text{PL photosynthesis}) = \min\left(\mu_{\text{N}}^{\text{PL}}, \mu_{\text{Si}}^{\text{PL}}, \mu_{\text{Fe}_d}^{\text{PL}}\right) L_{f,\text{PL}}(I) \\ \cdot \exp(k_{\text{PL}} T) [\text{PL}], \quad (\text{A23})$$

where  $\mu_{\text{N}}^{\text{PL}}$ ,  $\mu_{\text{Si}}^{\text{PL}}$  and  $\mu_{\text{Fe}_d}^{\text{PL}}$  are nitrogen ( $\text{NH}_4$  and  $\text{NO}_3$ ),  $\text{Si}(\text{OH})_4$  and  $\text{Fe}_d$  limited growth rates of PL, respectively,  $L_{f,\text{PL}}(I)$  is a non-dimensional light limiting factor for PL.  $\mu_{\text{N}}^{\text{PL}}$ ,  $\mu_{\text{Si}}^{\text{PL}}$  and  $\mu_{\text{Fe}_d}^{\text{PL}}$  are expressed in the following.

$$\mu_{\text{N}}^{\text{PL}} = \frac{V_{0,\text{PL}}[\text{NO}_3]}{\frac{[\text{NO}_3]}{1-f_{\text{AL}}} + \frac{V_{0,\text{PL}}}{f_{\text{AL}}A_{0,\text{NO}_3,\text{PL}}}} \left( 1 - \frac{[\text{NH}_4]}{[\text{NH}_4] + K_{\text{NH}_4,\text{PL}}} \right) + \frac{V_{0,\text{PL}}[\text{NH}_4]}{\frac{[\text{NH}_4]}{1-f_{\text{AL}}} + \frac{V_{0,\text{PL}}}{f_{\text{AL}}A_{0,\text{NH}_4,\text{PL}}}}, \quad (\text{A24})$$

$$\mu_{\text{Si}}^{\text{PL}} = \frac{V_{0,\text{PL}}[\text{Si}(\text{OH})_4]}{\frac{[\text{Si}(\text{OH})_4]}{1-f_{\text{AL}}} + \frac{V_{0,\text{PL}}}{f_{\text{AL}}A_{0,\text{Si,PL}}}}, \quad (\text{A25})$$

$$\mu_{\text{Fe}_d}^{\text{PL}} = \frac{V_{0,\text{PL}}[\text{Fe}_d]}{\frac{[\text{Fe}_d]}{1-f_{\text{AL}}} + \frac{V_{0,\text{PL}}}{f_{\text{AL}}A_{0,\text{Fe}_d,\text{PL}}}}, \quad (\text{A26})$$

where  $V_{0,\text{PL}}$ ,  $A_{0,\text{NO}_3,\text{PL}}$ ,  $A_{0,\text{NH}_4,\text{PL}}$ ,  $A_{0,\text{Si,PL}}$  and  $A_{0,\text{Fe}_d,\text{PL}}$  are the potential maximum growth rate of PL, and potential maximum affinity of PL for  $\text{NO}_3$ ,  $\text{NH}_4$ ,  $\text{Si}(\text{OH})_4$  and  $\text{Fe}_d$ , respectively and  $f_{\text{AL}}$  denotes the fraction of internal resources for nutrient uptake allocated to the cellular surface sites of PL. As for PL, the ratios of potential maximum affinities are set based on pre-existing estimates of Michaelis-Menten half-saturation constants,  $K_{\text{NO}_3,\text{PL}}$  ( $3.0 \mu\text{mol l}^{-1}$ ),  $K_{\text{NH}_4,\text{PL}}$  ( $0.3 \mu\text{mol l}^{-1}$ ),  $K_{\text{Si,PL}}$  ( $6.0 \mu\text{mol l}^{-1}$ ),  $K_{\text{Fe}_d,\text{PL}}$  ( $0.1 \text{nmol l}^{-1}$ ) as follows:

$$A_{0,\text{NH}_4,\text{PL}} = A_{0,\text{NO}_3,\text{PL}} \frac{K_{\text{NO}_3,\text{PL}}}{K_{\text{NH}_4,\text{PL}}}, \quad (\text{A27})$$

$$A_{0,\text{Si,PL}} = A_{0,\text{NO}_3,\text{PL}} \frac{K_{\text{NO}_3,\text{PL}}}{K_{\text{Si,PL}}}, \quad (\text{A28})$$

$$A_{0,\text{Fe}_d,\text{PL}} = A_{0,\text{NO}_3,\text{PL}} \frac{K_{\text{NO}_3,\text{PL}}}{K_{\text{Fe}_d,\text{PL}}}, \quad (\text{A29})$$

Equation (A30) for  $f_{\text{AL}}$  stipulates that acclimation occurs with respect to the limiting nutrient only.

$$f_{\text{AL}} = \max \left[ \left( 1 + \sqrt{\frac{\max(A_{0,\text{NO}_3,\text{PL}}[\text{NO}_3], A_{0,\text{NH}_4,\text{PL}}[\text{NH}_4])}{V_{0,\text{PL}}}} \right)^{-1}, \right. \\ \left. \left( 1 + \sqrt{\frac{A_{0,\text{Si,PL}}[\text{Si}(\text{OH})_4]}{V_{0,\text{PL}}}} \right)^{-1}, \left( 1 + \sqrt{\frac{A_{0,\text{Fe}_d,\text{PL}}[\text{Fe}_d]}{V_{0,\text{PL}}}} \right)^{-1} \right]. \quad (\text{A30})$$

For the non-dimensional light limiting factor of PL, the formula of *Platt et al.* [1980] is also used,

$$L_{f,\text{PL}}(I) = \frac{\left\{ 1 - \exp\left(-\frac{\alpha_{\text{PL}} I}{P_{\text{S,PL}}}\right) \right\} \exp\left(-\frac{\beta_{\text{PL}} I}{P_{\text{S,PL}}}\right)}{\left(\frac{\alpha_{\text{PL}}}{\alpha_{\text{PL}} + \beta_{\text{PL}}}\right) \left(\frac{\beta_{\text{PL}}}{\alpha_{\text{PL}} + \beta_{\text{PL}}}\right)^{\beta_{\text{PL}}/\alpha_{\text{PL}}}}. \quad (\text{A31})$$

F-ratio of PL ( $R_{\text{newL}}$ ) is defined as follows:

$$R_{\text{newL}} = \frac{\frac{V_{0,\text{PL}}[\text{NO}_3]}{\frac{[\text{NO}_3]}{1-f_{\text{AL}}} + \frac{V_{0,\text{PL}}}{f_{\text{AL}}A_{0,\text{NO}_3,\text{PL}}}} \left( 1 - \frac{[\text{NH}_4]}{[\text{NH}_4] + K_{\text{NH}_4,\text{PL}}} \right)}{\frac{V_{0,\text{PL}}[\text{NO}_3]}{\frac{[\text{NO}_3]}{1-f_{\text{AL}}} + \frac{V_{0,\text{PL}}}{f_{\text{AL}}A_{0,\text{NO}_3,\text{PL}}}} \left( 1 - \frac{[\text{NH}_4]}{[\text{NH}_4] + K_{\text{NH}_4,\text{PL}}} \right) + \frac{V_{0,\text{PL}}[\text{NH}_4]}{\frac{[\text{NH}_4]}{1-f_{\text{AL}}} + \frac{V_{0,\text{PL}}}{f_{\text{AL}}A_{0,\text{NH}_4,\text{PL}}}}}. \quad (\text{A32})$$

Light intensity at the depth  $z$  used in equations (A21) and (A31) is represented as follows:

$$I = I_0 \exp\left(-\int_0^z \kappa dz\right), \quad (\text{A33})$$

$$\kappa = \alpha_1 + \alpha_2([\text{PS}] + [\text{PL}]), \quad (\text{A34})$$

where  $I_0$  is the irradiance at the sea surface, imposed as a boundary condition, and  $\kappa$  is the light extinction coefficient.

[42] The formulae used for respiration, extracellular excretion and mortality of phytoplankton, PS and PL, and

mortality of zooplankton, ZS, ZL and ZP are the same as the previous model and read:

$$(\text{PS respiration}) = R_{\text{PS}0} \exp(k_{\text{RS}} T) [\text{PS}], \quad (\text{A35})$$

$$(\text{PL respiration}) = R_{\text{PL}0} \exp(k_{\text{RL}} T) [\text{PL}], \quad (\text{A36})$$

$$(\text{PS extracellular excretion}) = \gamma_{\text{S}} (\text{PS photosynthesis}), \quad (\text{A37})$$

$$(\text{PL extracellular excretion}) = \gamma_{\text{L}} (\text{PL photosynthesis}), \quad (\text{A38})$$

$$(\text{PS mortality}) = M_{\text{PS}0} \exp(k_{\text{MS}} T) [\text{PS}]^2, \quad (\text{A39})$$

$$(\text{PL mortality}) = M_{\text{PL}0} \exp(k_{\text{ML}} T) [\text{PL}]^2, \quad (\text{A40})$$

$$(\text{ZS mortality}) = M_{\text{ZS}0} \exp(k_{\text{MZS}} T) [\text{ZS}]^2, \quad (\text{A41})$$

$$(\text{ZL mortality}) = M_{\text{ZL}0} \exp(k_{\text{MZL}} T) [\text{ZL}]^2, \quad (\text{A42})$$

$$(\text{ZP mortality}) = M_{\text{ZP}0} \exp(k_{\text{MZP}} T) [\text{ZP}]^2. \quad (\text{A43})$$

As in the previous model, grazing and predation by zooplankton are derived from the formulae:

$$(\text{PS grazing by ZS}) = G_{\text{RmaxS}} \max \left[ 0, 1 - \exp \left\{ \lambda_{\text{S}} \left( \text{PS}_{\text{ZS}}^* - [\text{PS}] \right) \right\} \right] \times \exp(k_{\text{GS}} T) [\text{ZS}], \quad (\text{A44})$$

$$(\text{PS grazing by ZL}) = G_{\text{RmaxL,PS}} \max \left[ 0, 1 - \exp \left\{ \lambda_{\text{L}} \left( \text{PS}_{\text{ZL}}^* - [\text{PS}] \right) \right\} \right] \times \exp(k_{\text{GL}} T) [\text{ZL}], \quad (\text{A45})$$

$$(\text{PL grazing by ZL}) = G_{\text{RmaxL,PL}} \max \left[ 0, 1 - \exp \left\{ \lambda_{\text{L}} \left( \text{PL}_{\text{ZL}}^* - [\text{PL}] \right) \right\} \right] \times \exp(k_{\text{GL}} T) [\text{ZL}], \quad (\text{A46})$$

$$(\text{ZS predation by ZL}) = G_{\text{RmaxL,ZS}} \max \left[ 0, 1 - \exp \left\{ \lambda_{\text{L}} \left( \text{ZS}_{\text{ZL}}^* - [\text{ZS}] \right) \right\} \right] \times \exp(k_{\text{GL}} T) [\text{ZL}], \quad (\text{A47})$$

$$(\text{PL grazing by ZP}) = G_{\text{RmaxP,PL}} \max \left[ 0, 1 - \exp \left\{ \lambda_{\text{P}} \left( \text{PL}_{\text{ZP}}^* - [\text{PL}] \right) \right\} \right] \times \exp \left\{ -\Psi_{\text{PL}} ([\text{ZS}] + [\text{ZL}]) \right\} \exp(k_{\text{GP}} T) [\text{ZP}], \quad (\text{A48})$$

$$(\text{ZS predation by ZP}) = G_{\text{RmaxP,ZS}} \max \left[ 0, 1 - \exp \left\{ \lambda_{\text{P}} \left( \text{ZS}_{\text{ZP}}^* - [\text{ZS}] \right) \right\} \right] \times \exp(-\Psi_{\text{ZS}} [\text{ZL}]) \exp(k_{\text{GP}} T) [\text{ZP}], \quad (\text{A49})$$

$$(\text{ZL predation by ZP}) = G_{\text{RmaxP,ZL}} \max \left[ 0, 1 - \exp \left\{ \lambda_{\text{P}} \left( \text{ZL}_{\text{ZP}}^* - [\text{ZL}] \right) \right\} \right] \times \exp(k_{\text{GP}} T) [\text{ZP}]. \quad (\text{A50})$$

Excretion and egestion for ZS, ZL and ZP are also the same as in the previous model and read:

$$(\text{ZS excretion}) = (\alpha_{\text{ZS}} - \beta_{\text{ZS}}) (\text{PS grazing by ZS}), \quad (\text{A51})$$

$$(\text{ZL excretion}) = (\alpha_{\text{ZL}} - \beta_{\text{ZL}}) \{ (\text{PS grazing by ZL}) + (\text{PL grazing by ZL}) + (\text{ZS predation by ZL}) \}, \quad (\text{A52})$$

$$(\text{ZP excretion}) = (\alpha_{\text{ZP}} - \beta_{\text{ZP}}) \{ (\text{PL grazing by ZP}) + (\text{ZS predation by ZP}) + (\text{ZL predation by ZP}) \}, \quad (\text{A53})$$

$$(\text{ZS egestion}) = (1 - \alpha_{\text{ZS}}) (\text{PS grazing by ZS}), \quad (\text{A54})$$

$$(\text{ZL egestion}) = (1 - \alpha_{\text{ZL}}) \{ (\text{PS grazing by ZL}) + (\text{PL grazing by ZL}) + (\text{ZS predation by ZL}) \}, \quad (\text{A55})$$

$$(\text{ZP egestion}) = (1 - \alpha_{\text{ZP}}) \{ (\text{PL grazing by ZP}) + (\text{ZS predation by ZP}) + (\text{ZL predation by ZP}) \}. \quad (\text{A56})$$

As in the previous model, decomposition and remineralization of  $\text{PON}_{\text{S}}$ ,  $\text{PON}_{\text{L}}$ , DON and Opal and nitrification are formulated as follows:

$$(\text{PON}_{\text{S}} \text{ remineralization}) = V_{\text{PA}0\text{S}} \exp(k_{\text{PAS}} T) [\text{PON}_{\text{S}}], \quad (\text{A57})$$

$$(\text{PON}_{\text{S}} \text{ decomposition to DON}) = V_{\text{PD}0\text{S}} \exp(k_{\text{PDS}} T) [\text{PON}_{\text{S}}], \quad (\text{A58})$$

$$(\text{PON}_{\text{L}} \text{ remineralization}) = V_{\text{PA}0\text{L}} \exp(k_{\text{PAL}} T) [\text{PON}_{\text{L}}], \quad (\text{A59})$$

$$(\text{PON}_{\text{L}} \text{ decomposition to DON}) = V_{\text{PD}0\text{L}} \exp(k_{\text{PDL}} T) [\text{PON}_{\text{L}}], \quad (\text{A60})$$

$$(\text{DON remineralization}) = V_{\text{DA}0} \exp(k_{\text{DA}} T) [\text{DON}], \quad (\text{A61})$$

$$(\text{Opal dissolution}) = V_{\text{Opal}} \exp(k_{\text{Opal}} T) [\text{Opal}], \quad (\text{A62})$$

$$(\text{Nitrification}) = V_{\text{Nit}0} \exp(k_{\text{Nit}} T) [\text{NH}_4], \quad (\text{A63})$$

Although PON is divided into two classes in the present model, the specific decomposition and remineralization rates are assumed to be the same.

[43] The equations for the biogenic opal (Opal) are also the same as in the previous model, except for settling.

$$(\text{Opal formation}) = \{ (\text{PL photosynthesis}) - (\text{PL respiration}) - (\text{PL extracellular excretion}) \} \times R_{\text{SiN}}, \quad (\text{A64})$$

$$(\text{Opal derived from PL mortality}) = (\text{PL mortality}) \times R_{\text{SiN}}, \quad (\text{A65})$$

$$(\text{Opal egestion by ZL}) = (\text{PL grazing by ZL}) \times R_{\text{SiN}}, \quad (\text{A66})$$

$$(\text{Opal egestion by ZP}) = (\text{PL grazing by ZP}) \times R_{\text{SiN}}. \quad (\text{A67})$$

$R_{\text{SiN}}$  is determined by the surrounding dissolved iron concentration because in the iron deficient condition diatoms tend to uptake the silicate and nitrate in higher Si:N ratio than that in the iron rich condition [e.g., *Takeda*, 1998]. That is simply formulated as follows:

$$R_{\text{SiN}} = \begin{cases} R_{\text{SiNH}} ([\text{Fe}_d] \geq \text{Fe}_{\text{SiN}}^*) \\ R_{\text{SiNL}} ([\text{Fe}_d] < \text{Fe}_{\text{SiN}}^*) \end{cases} \quad (\text{A68})$$

The aggregation processes between DON,  $\text{PON}_S$  and  $\text{PON}_L$  due to turbulence and differential settling are considered based on the parameterization proposed by *Aumont and Bopp* [2006] as follows:

$$\begin{aligned} (\text{Aggregation for DON to } \text{PON}_S) &= \phi_1^{\text{DON}} \text{sh}[\text{DON}]^2 \\ &+ \phi_2^{\text{DON}} \text{sh}[\text{DON}][\text{PON}_S], \end{aligned} \quad (\text{A69})$$

$$\begin{aligned} (\text{Dust dissolution}) &= \begin{cases} 0.01 \alpha F_{0, \text{Fe}_{\text{dust}}} / \Delta z_s - \left( \frac{\partial F_{\text{Fe}_{\text{soft}_{\text{dust}}}}}{\partial z} + \frac{\partial F_{\text{Fe}_{\text{hard}_{\text{dust}}}}}{\partial z} \right) & (\text{top - most layer}) \\ - \left( \frac{\partial F_{\text{Fe}_{\text{soft}_{\text{dust}}}}}{\partial z} + \frac{\partial F_{\text{Fe}_{\text{hard}_{\text{dust}}}}}{\partial z} \right) & (\text{elsewhere}), \end{cases} \end{aligned} \quad (\text{A76})$$

$$(\text{Aggregation for DON to } \text{PON}_L) = \phi_3^{\text{DON}} \text{sh}[\text{DON}][\text{PON}_L], \quad (\text{A70})$$

$$\begin{aligned} (\text{Aggregation for } \text{PON}_S \text{ to } \text{PON}_L) &= \phi_1^{\text{PON}_S} \text{sh}[\text{PON}_S]^2 \\ &+ \phi_2^{\text{PON}_S} \text{sh}[\text{PON}_S][\text{PON}_L] + \phi_3^{\text{PON}_S} [\text{PON}_S]^2 \\ &+ \phi_4^{\text{PON}_S} [\text{PON}_S][\text{PON}_L]. \end{aligned} \quad (\text{A71})$$

In (A69) to (A71), sh depicts the shear rate which was set at  $1 \text{ s}^{-1}$  in the mixed layer and at  $0.01 \text{ s}^{-1}$  elsewhere.

[44] The sinking of particles is described as follows:

$$(\text{PON}_S \text{ settlement}) = -w^{\text{PON}_S} \frac{\partial [\text{PON}_S]}{\partial z}, \quad (\text{A72})$$

$$(\text{PON}_L \text{ settlement}) = -\frac{\partial (w^{\text{PON}_L} [\text{PON}_L])}{\partial z}, \quad (\text{A73})$$

$$(\text{Opal settlement}) = -\frac{\partial (w^{\text{Opal}} [\text{Opal}])}{\partial z}. \quad (\text{A74})$$

The sinking speed of  $\text{PON}_L$ ,  $w^{\text{PON}_L}$ , increases with depth as in *Aumont and Bopp* [2006] and reads:

$$w^{\text{PON}_L} = w_{\text{min}}^{\text{PON}_L} + \left( w_{\text{max}}^{\text{PON}_L} - w_{\text{min}}^{\text{PON}_L} \right) \times \left( \frac{z - z_{\text{MLD}}}{2000} \right). \quad (\text{A75})$$

where  $z_{\text{MLD}}$  is the depth of the mixed layer. So far, the sinking rate of Opal ( $w^{\text{Opal}}$ ) is the same as that of  $\text{PON}_L$ , and thus Opal settles at the same sinking speed as  $\text{PON}_L$ .

[45] The formulae used for  $\text{Fe}_d$  and  $\text{Fe}_p$  are basically derived from the parameterization of *Moore et al.* [2004] and *Moore and Braucher* [2008]. In terms of  $\text{Fe}_p$  desorption, we considered Arrhenius type temperature dependency. The settlement of  $\text{Fe}_p$  differs from the previous researches treating that as instantaneously sinking matter. However, dust is treated as instantaneously sinking matter as in the previous researches.

where  $F_{0, \text{Fe}_{\text{dust}}}$  is the dust-derived iron flux as the boundary condition and calculated using iron content ( $C_{\text{iron}}$ ) of 3.5% in dust, iron atomic weight ( $A_{w, \text{Fe}}$ ) and prescribed dust flux ( $F_{0, \text{dust}}$ ).  $\alpha$  is the % solubility of iron in dust, and  $\Delta z_s$  is the thickness of the model's top-most layer. All the soluble iron is treated as bioavailable one. As in the previous researches, left dust-derived iron flux is separated into two components, labile ( $F_{\text{Fe}_{\text{soft}_{\text{dust}}}}$ ) and refractory ( $F_{\text{Fe}_{\text{hard}_{\text{dust}}}}$ ) ones, and the fluxes at a given depth ( $z$ ) are considered with different length scale ( $\delta_{\text{soft}_{\text{dust}}}$ ,  $\delta_{\text{hard}_{\text{dust}}}$ ) as follows:

$$F_{\text{Fe}_{\text{soft}_{\text{dust}}}}(z) = F_{0, \text{Fe}_{\text{dust}}} (1 - 0.01 \alpha) (1 - f_{\text{hard}}) e^{-\frac{z}{\delta_{\text{soft}_{\text{dust}}}}}, \quad (\text{A77})$$

$$F_{\text{Fe}_{\text{hard}_{\text{dust}}}}(z) = F_{0, \text{Fe}_{\text{dust}}} (1 - 0.01 \alpha) f_{\text{hard}} e^{-\frac{z}{\delta_{\text{hard}_{\text{dust}}}}}. \quad (\text{A78})$$

Dust is also treated as above in the model to reduce the computational cost of running the model, but the dust flux at a given depth is involved in the below scavenging process.

[46] The scavenging of  $\text{Fe}_d$ , desorption and settlement of  $\text{Fe}_p$  are formulated as follows:

$$(\text{Fe}_d \text{ scavenging}) = \begin{cases} f_{\text{Fe}_p} \lambda_{\text{scav}} (F_{\text{POC}} + F_{\text{dust}}) [\text{Fe}_d] & ([\text{Fe}_d] < C_{\text{ligand}} (0.6 \text{ nM})) \\ f_{\text{Fe}_p} \left\{ \lambda_{\text{scav}} (F_{\text{POC}} + F_{\text{dust}}) [\text{Fe}_d] + \gamma_{\text{high}} ([\text{Fe}_d] - C_{\text{ligand}}) \right\} [\text{Fe}_d] & ([\text{Fe}_d] \geq C_{\text{ligand}} (0.6 \text{ nM})) \end{cases}, \quad (\text{A79})$$

$$(\text{Fe}_d \text{ burial}) = \begin{cases} (1 - f_{\text{Fe}_p}) \lambda_{\text{scav}} (F_{\text{POC}} + F_{\text{dust}}) [\text{Fe}_d] & ([\text{Fe}_d] < C_{\text{ligand}} (0.6 \text{ nM})) \\ (1 - f_{\text{Fe}_p}) \left\{ \lambda_{\text{scav}} (F_{\text{POC}} + F_{\text{dust}}) [\text{Fe}_d] + \gamma_{\text{high}} ([\text{Fe}_d] - C_{\text{ligand}}) \right\} [\text{Fe}_d] & ([\text{Fe}_d] \geq C_{\text{ligand}} (0.6 \text{ nM})) \end{cases}, \quad (\text{A80})$$

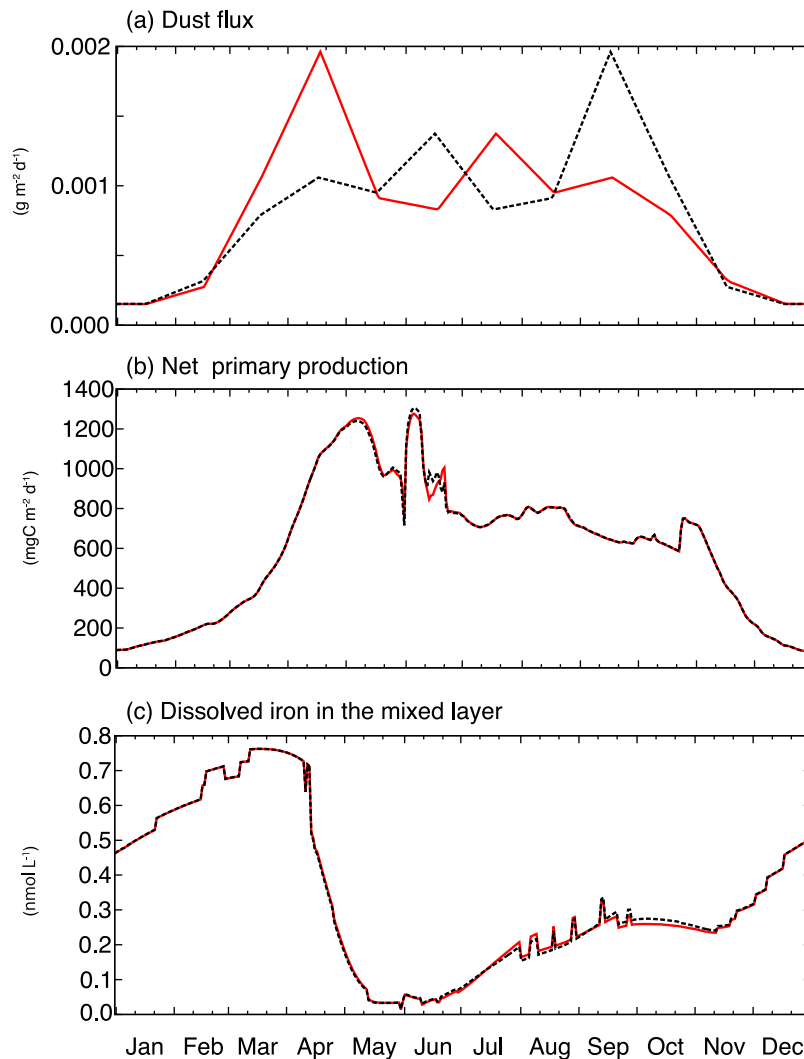


**Figure B1.** Comparisons between the simulated results with the control dust forcing and that of which seasonality was changed. (a) Dust forcing ( $\text{g m}^{-2} \text{d}^{-1}$ ), (b) net primary production, and (c) dissolved iron averaged in the mixed layer. In Figure B1a, line in red represents the new dust forcing of which seasonal variation is changed from that in the control case (line in black). As for the new dust forcing, the annual load of dust deposition is kept at the same one as the control case. In Figures B1b and B1c, lines in red represent the results with the new dust forcing and those in black denote the control case results.

$$(\text{Fe}_p \text{ desorption}) = \lambda_{\text{desorption}} \exp\left\{-A_E \left(\frac{1}{T} - \frac{1}{T_{\text{ref}}}\right)\right\} [\text{Fe}_p], \quad (\text{A81})$$

$$(\text{Fe}_p \text{ settlement}) = -w_{\text{Fep}} \frac{\partial [\text{Fe}_p]}{\partial z}. \quad (\text{A82})$$

In A79 and A80,  $F_{\text{POC}}$  and  $F_{\text{dust}}$  represent the fluxes of POC and dust at a given depth, respectively, and  $C_{\text{ligand}}$  is the prescribed total ligand concentration (0.6nM).  $F_{\text{POC}}$  is converted from PON flux with  $R_{\text{CN}}$ .

## Appendix B

[47] As mentioned in section 3.1, we performed an additional simulation to confirm if the difference in seasonality

of dust forcing can affect the biogeochemistry in the upper ocean or not. The difference between the new dust forcing and control one is whether there is the dust flux peak in fall or spring. As a result, there is not much difference in the result of simulated biogeochemical components, such as net primary production (NPP), nutrients and dissolved ( $\text{Fe}_d$ ) and particulate iron between the additional and control ones (the results of NPP and  $\text{Fe}_d$  for each simulation shown in Figure B1 with each dust forcing). The reason behind that seems to be as follows:

[48] 1. In spring, a plentiful  $\text{Fe}_d$  supplied to the mixed layer during winter by the vertical mixing still remains unused, and the  $\text{Fe}_d$  makes the contribution of dust-derived iron to the surface  $\text{Fe}_d$  concentration small (Figure 6).

[49] 2. In fall, phytoplankton is limited by not  $\text{Fe}_d$  but nitrogenous nutrients (Figure 5), and dust-derived iron has little impact on the surface biogeochemistry.

[50] Thus, the presently used dust forcing appears to be different from observations, but that does not influence the simulated results with the forcing very much, at least for the present experimental design.

[51] **Acknowledgments.** We thank the anonymous reviewers for their various valuable comments, which improved our manuscript. This work was partially supported by CREST/JST and the Grant-in-Aid for Scientific Research in Priority Areas “Western Pacific Air-Sea Interaction Study (W-PASS)” under grant 18067004.

## References

- Aita, M. N., Y. Yamanaka, and M. J. Kishi (2007), Interdecadal variation of the lower trophic ecosystem in the northern Pacific between 1948 and 2002, in a 3-D implementation of the NEMURO model, *Ecol. Modell.*, *202*, 81–94, doi:10.1016/j.ecolmodel.2006.07.045.
- Armstrong, R. A., C. Lee, J. I. Hedges, S. Honjo, and S. G. Wakeham (2002), A new, mechanistic model for organic carbon fluxes in the ocean based on the quantitative association of POC with ballast minerals, *Deep Sea Res., Part II*, *49*, 219–236, doi:10.1016/S0967-0645(01)00101-1.
- Aumont, O., and L. Bopp (2006), Globalizing results from ocean in situ iron fertilization studies, *Global Biogeochem. Cycles*, *20*, GB2017, doi:10.1029/2005GB002591.
- Berelson, W. M. (2002), Particle settling rates increase with depth in the ocean, *Deep Sea Res., Part II*, *49*, 237–251, doi:10.1016/S0967-0645(01)00102-3.
- Bergquist, B. A., and E. A. Boyle (2006), Dissolved iron in the tropical and subtropical Atlantic Ocean, *Global Biogeochem. Cycles*, *20*, GB1015, doi:10.1029/2005GB002505.
- Fasham, M. J. R., H. W. Ducklow, and S. M. McKelvie (1990), A nitrogen-based model of plankton dynamics in the oceanic mixed layer, *J. Mar. Res.*, *48*, 591–639.
- Franck, V. M., M. A. Brzezinski, K. H. Coale, and D. M. Nelson (2000), Iron and silicic acid concentrations regulate Si uptake north and south of the Polar Frontal Zone in the Pacific sector of the Southern Ocean, *Deep Sea Res., Part II*, *47*, 3315–3338, doi:10.1016/S0967-0645(00)00070-9.
- Franck, V. M., K. W. Bruland, D. A. Hutchins, and M. A. Brzezinski (2003), Iron and zinc effects on silicic acid and nitrate uptake kinetics in three high-nutrient, low-chlorophyll (HNLC) regions, *Mar. Ecol. Prog. Ser.*, *252*, 15–33, doi:10.3354/meps252015.
- Fujii, M., Y. Yamanaka, Y. Nojiri, M. J. Kishi, and F. Chai (2007), Comparison of seasonal characteristics in biogeochemistry among the subarctic North Pacific stations described with a NEMURO-based marine ecosystem model, *Ecol. Modell.*, *202*, 52–67, doi:10.1016/j.ecolmodel.2006.02.046.
- Hurst, M. P., and K. W. Bruland (2007), An investigation into the exchange of iron and zinc between soluble, colloidal, and particulate size-fractions in shelf waters using low-abundance isotopes as tracers in shipboard incubation experiments, *Mar. Chem.*, *103*, 211–226, doi:10.1016/j.marchem.2006.07.001.
- Kishi, M. J., et al. (2007), NEMURO—a lower trophic level model for the North Pacific marine ecosystem, *Ecol. Modell.*, *202*, 12–25, doi:10.1016/j.ecolmodel.2006.08.021.
- Kondo, Y., S. Takeda, J. Nishioka, H. Obata, K. Furuya, W. K. Johnson, and C. S. Wong (2008), Organic iron (III) complexing ligand during an iron enrichment experiment in the western subarctic North Pacific, *Geophys. Res. Lett.*, *35*, L12601, doi:10.1029/2008GL033354.
- Krishnakumar, K. (1989), Micro-genetic algorithms for stationary and non-stationary function optimization, *Intel. Control Adaptive Syst.*, *1196*, 289–296.
- Kudo, I., Y. Noiri, J. Nishioka, Y. Taira, H. Kiyosawa, and A. Tsuda (2006), Phytoplankton community response to Fe and temperature gradients in the NE (SERIES) and NW (SEEDS) subarctic Pacific Ocean, *Deep Sea Res., Part II*, *53*, 2201–2213, doi:10.1016/j.dsr2.2006.05.033.
- Lancelot, C., E. Hannon, S. Becquevort, C. Veth, and H. J. W. De Baar (2000), Modeling phytoplankton blooms and carbon export production in the Southern Ocean: Dominant controls by light and iron in the Atlantic sector in Austral spring 1992, *Deep Sea Res., Part I*, *47*, 1621–1662, doi:10.1016/S0967-0637(00)00005-4.
- Levitus, S. (1982), Climatological atlas of the world ocean, *NOAA Prof. Pap.* *13*, 191 pp., NOAA, Rockville, Md.
- Logan, B. E., and J. R. Hunt (1987), Advantages to microbes of growth in permeable aggregates in marine systems, *Limnol. Oceanogr.*, *32*, 1034–1048, doi:10.4319/lo.1987.32.5.1034.
- Martin, J. H., R. M. Gordon, S. Fitzwater, and W. W. Broenkow (1989), VERTEX: Phytoplankton/iron studies in the Gulf of Alaska, *Deep Sea Res., Part I*, *36*(5), 649–680, doi:10.1016/0198-0149(89)90144-1.
- Martin-Jézéquel, V., M. Hildebrand, and M. A. Brzezinski (2000), Silicon-metabolism in diatoms: Implications for growth, *J. Phycol.*, *36*, 821–840, doi:10.1046/j.1529-8817.2000.00019.x.
- Measures, C. I., M. T. Brown, and S. Vink (2005), Dust deposition to the surface waters of the western and central North Pacific inferred from surface water dissolved aluminum concentrations, *Geochem. Geophys. Geosyst.*, *6*, Q09M03, doi:10.1029/2005GC000922.
- Mills, M. M., C. Ridame, M. Davey, J. La Roche, and R. J. Geider (2004), Iron and phosphorus co-limit nitrogen fixation in the eastern tropical North Atlantic, *Nature*, *429*(6989), 292–294, doi:10.1038/nature02550.
- Misumi, K., et al. (2011), Mechanisms controlling dissolved iron distribution in the North Pacific: A model study, *J. Geophys. Res.*, *116*, G03005, doi:10.1029/2010JG001541.
- Mochizuki, T., et al. (2010), Pacific decadal oscillation hindcasts relevant to near-term climate prediction, *Proc. Natl. Acad. Sci. U. S. A.*, *107*, 1833–1837, doi:10.1073/pnas.0906531107.
- Moore, J. K., and O. Braucher (2008), Sedimentary and mineral dust sources of dissolved iron to the world ocean, *Biogeosciences*, *5*(3), 631–656, doi:10.5194/bg-5-631-2008.
- Moore, J. K., S. C. Doney, and K. Lindsay (2004), Upper ocean ecosystem dynamics and iron cycling in a global three-dimensional model, *Global Biogeochem. Cycles*, *18*, GB4028, doi:10.1029/2004GB002220.
- Nishioka, J., et al. (2007), Iron supply to the western subarctic Pacific: Importance of iron export from the Sea of Okhotsk, *J. Geophys. Res.*, *112*, C10012, doi:10.1029/2006JC004055.
- Nishioka, J., T. Ono, H. Saito, K. Sakaoka, and T. Yoshimura (2011), Oceanic iron supply mechanisms which support the spring diatom bloom in the Oyashio region, western subarctic Pacific, *J. Geophys. Res.*, *116*, C02021, doi:10.1029/2010JC006321.
- Ohtani, K. (1989), The role of the Sea of Okhotsk on the formation of the Oyashio water [in Japanese with English abstract], *Uni to Sora*, *65*(2), 63–83.
- Ooki, A., J. Nishioka, T. Ono, and S. Noriki (2009), Size dependence of iron solubility of Asian mineral dust particles, *J. Geophys. Res.*, *114*, D03202, doi:10.1029/2008JD010804.
- Parekh, P., M. J. Follows, and E. Boyle (2004), Modeling the global ocean iron cycle, *Global Biogeochem. Cycles*, *18*, GB1002, doi:10.1029/2003GB002061.
- Platt, T., C. L. Gallegos, and W. G. Harrison (1980), Photoinhibition of photosynthesis in natural assemblages of marine phytoplankton, *J. Mar. Res.*, *38*, 687–701.
- Saito, H., A. Tsuda, and H. Kasai (2002), Nutrient and plankton dynamics in the Oyashio region of the western subarctic Pacific Ocean, *Deep Sea Res., Part II*, *49*, 5463–5486, doi:10.1016/S0967-0645(02)00204-7.
- Sarthou, G., et al. (2003), Atmospheric iron deposition and sea-surface dissolved iron concentrations in the eastern Atlantic Ocean, *Deep Sea Res., Part I*, *50*, 1339–1352, doi:10.1016/S0967-0637(03)00126-2.
- Scarratt, M. G., et al. (2006), Assessing microbial responses to iron enrichment in the Subarctic Northeast Pacific: Do microcosms reproduce the in situ condition?, *Deep Sea Res., Part II*, *53*, 2182–2200, doi:10.1016/j.dsr2.2006.05.035.
- Schartau, M., and A. Oschlies (2003), Simultaneous data-based optimization of a 1D-ecosystem model at three locations in the North Atlantic: Part I—Method and parameter estimates, *J. Mar. Res.*, *61*, 765–793, doi:10.1357/002224003322981147.
- Smith, S. L. (2010), Untangling the uncertainties about combined effects of temperature and concentration on nutrient uptake rates in the ocean, *Geophys. Res. Lett.*, *37*, L11603, doi:10.1029/2010GL043617.
- Smith, S. L. (2011), Consistently modeling the combined effects of temperature and concentration on nitrate uptake in the ocean, *J. Geophys. Res.*, *116*, G04020, doi:10.1029/2011JG001681.
- Smith, S. L., and Y. Yamanaka (2007), Optimization-based model of multi-nutrient uptake kinetics, *Limnol. Oceanogr.*, *52*(4), 1545–1558, doi:10.4319/lo.2007.52.4.1545.
- Smith, S. L., Y. Yamanaka, M. Pahlow, and A. Oschlies (2009), Optimal uptake kinetics: Physiological acclimation explains the pattern of nitrate uptake by phytoplankton in the ocean, *Mar. Ecol. Prog. Ser.*, *384*, 1–12, doi:10.3354/meps08022.
- Steele, J. H. (1962), Environmental control of photosynthesis in the sea, *Limnol. Oceanogr.*, *7*, 137–150, doi:10.4319/lo.1962.7.2.0137.
- Sumata, H., et al. (2010), Effect of eddy transport on the nutrient supply into the euphotic zone simulated in an eddy-permitting ocean ecosystem model, *J. Mar. Syst.*, *83*, 67–87, doi:10.1016/j.jmarsys.2010.07.002.
- Takeda, S. (1998), Influence of iron availability on nutrient consumption ratio of diatoms in oceanic waters, *Nature*, *393*, 774–777, doi:10.1038/31674.
- Takeda, S., N. Yoshie, P. W. Boyd, and Y. Yamanaka (2006), Modeling studies investigating the causes of preferential depletion of silicic acid relative to nitrate during SERIES, a mesoscale iron enrichment in the

- NE subarctic Pacific, *Deep Sea Res., Part II*, 53, 2297–2326, doi:10.1016/j.dsr2.2006.05.027.
- Tsuda, A., et al. (2003), A mesoscale iron enrichment in the western subarctic Pacific induces large centric diatom bloom, *Science*, 300, 958–961, doi:10.1126/science.1082000.
- Uematsu, M., Z. Wang, and I. Uno (2003), Atmospheric input of mineral dust to the western North Pacific region based on direct measurements and a regional chemical transport model, *Geophys. Res. Lett.*, 30(6), 1342, doi:10.1029/2002GL016645.
- Vallina, S. M., and C. Le Quéré (2008), Preferential uptake of  $\text{NH}_4^+$  over  $\text{NO}_3^-$  in marine ecosystem models: A simple and more consistent parameterization, *Ecol. Modell.*, 218, 393–397, doi:10.1016/j.ecolmodel.2008.06.038.
- Yamanaka, Y., N. Yoshie, M. Fujii, M. N. Aita, and M. J. Kishi (2004), An ecosystem model coupled with nitrogen-silicon-carbon cycles applied to station A7 in the northwestern Pacific, *J. Oceanogr.*, 60, 227–241, doi:10.1023/B:JOCE.0000038329.91976.7d.
- Yokouchi, K., et al. (2007), Simulated *in situ* measurements of primary production in Japanese waters, in *Global Climate Change and Response of Carbon Cycle in the Equatorial Pacific and Indian Oceans and Adjacent Landmasses*, edited by H. Kawahata and Y. Awaya, *Elsevier Oceanogr. Ser.*, 73, 65–88, doi:10.1016/S0422-9894(06)73003-3.
- Zhu, X. R., J. M. Prospero, and F. J. Millero (1997), Diel variability of soluble Fe(II) and soluble total Fe in North African dust in the trade winds at Barbados, *J. Geophys. Res.*, 102, 21,297–21,305, doi:10.1029/97JD01313.